

---

# **Numerical Solution of the Incompressible Navier-Stokes Equations in Three-Dimensional Generalized Curvilinear Coordinates**

---

Stuart E. Rogers, Dochan Kwak, and James L.C.  
Chang

---

January 1986



National Aeronautics and  
Space Administration



---

# **Numerical Solution of the Incompressible Navier-Stokes Equations in Three-Dimensional Generalized Curvilinear Coordinates**

---

Stuart E. Rogers,  
Dochan Kwak, Ames Research Center, Moffett Field, California  
James L. C. Chang, Rocketdyne Division, Canoga Park, California

January 1986



National Aeronautics and  
Space Administration

**Ames Research Center**  
Moffett Field, California 94035



# NUMERICAL SOLUTION OF THE INCOMPRESSIBLE NAVIER-STOKES EQUATIONS IN THREE-DIMENSIONAL GENERALIZED CURVILINEAR COORDINATES

Stuart E. Rogers and Dochan Kwak  
Ames Research Center

James L. C. Chang  
Rocketdyne Division, Rockwell International  
Canoga Park, California

## SUMMARY

Numerically solving the incompressible Navier-Stokes equations is known to be time-consuming and expensive. Testing of the INS3D computer code, which solves these equations with the use of the pseudocompressibility method, shows this method to be an efficient way to obtain the steady-state solution. The effects of the waves introduced by the pseudocompressibility method are analyzed and criteria are set and tested for the choice of the pseudocompressibility parameter which governs the artificial sound speed. The code is tested using laminar flow over a two-dimensional backward-facing step, and laminar flow over a two-dimensional circular cylinder. The results of the computations over the backward-facing step are in excellent agreement with experimental results. The transient solution of the flow over the cylinder impulsively started from rest is in good agreement with experimental results. However, the computed frequency of periodic shedding of vortices behind the cylinder is not in agreement with the experimental value. For a three-dimensional test case, computations were conducted for a cylinder-end wall junction. The saddle point separation and horseshoe vortex system appear in the computed flow field. The solution also shows secondary vortex filaments which wrap around the cylinder and spiral up in the wake.

## INTRODUCTION

Computational fluid dynamics (CFD) is rapidly advancing both as a tool for theoretical study and as a tool for engineering design. This is partly due to the increasing power and efficiency of the high-speed supercomputer. It has, therefore, become feasible to numerically simulate complicated fluid-flow phenomena associated with complex geometries. Thus, one of the primary pacing items in computational fluid dynamics research is the development of new solution methodologies (ref. 1). This paper is the result of research at NASA Ames Research Center in coordination with the development of a three-dimensional, incompressible, Navier-Stokes solver utilizing primitive variables and generalized curvilinear coordinates.

## PURPOSE OF THE STUDY

There are many important incompressible flow problems in engineering applications, some of which include hydrodynamics, liquid fuel flows in propulsion, and low-speed air flow. When the flow is two-dimensional in nature, there are several efficient methods for numerically solving the incompressible Navier-Stokes equations. These flow solvers do not significantly impact a supercomputer's memory and time constraints because two-dimensional flow fields have small data base requirements, e.g., the stream function-vorticity formulation is one popular method (refs. 2-5). However, many incompressible viscous flows are highly three-dimensional in nature and there is no straightforward three-dimensional extension to this method; therefore, the use

Funds for the support the first author in this study have been allocated by the NASA-Ames Research Center, Moffett Field, California, under Interchange No. NCA2-OR170-302.

of primitive variables (velocities and pressure) is preferred. There are several three-dimensional codes which solve the compressible Navier-Stokes equations, examples of which are given by references 6 - 9. Since the speed of sound approaches infinity at the incompressible limit, it is not computationally efficient to use these codes for computing incompressible flows. Therefore, there is a need for an efficient three-dimensional incompressible Navier-Stokes solver which can be used for a realistic three-dimensional geometry.

## SOLVING THE INCOMPRESSIBLE NAVIER-STOKES EQUATIONS

One of the major concerns in numerically solving the incompressible Navier-Stokes equations in primitive variable form is the method used for evaluating the pressure. The pressure does not explicitly appear in the continuity equation yet it acts as a dynamic parameter in ensuring that continuity is satisfied, and that the velocity field is divergence-free. One method that was developed by Harlow and Welch (ref. 10), for use with their MAC (marker and cell) code, involves the solution of a Poisson equation for pressure. By taking the divergence of the momentum equations, a Poisson equation in pressure is derived. In using this method, the normal time-advancement would be as follows: the momentum equations are solved for the velocities, then the Poisson equation is solved for the pressure which ensures a divergence-free flow at the next time-step. The solution of the Poisson equation usually requires a relaxation scheme to iterate on pressure until the divergence-free condition is reasonably satisfied. This method has been widely used, particularly for solving two-dimensional problems, (refs. 11 - 17). However, the solution of the Poisson equation can be prohibitively time-consuming for three-dimensional problems.

In his 1968 paper, Chorin (ref. 18) presents the basis for applying the fractional step method in solving the incompressible Navier-Stokes equations. The theoretical basis can be found in another paper by Chorin (ref. 19) and in the book by Temam (ref. 20). The essential mechanics are as follows: in the computation the time-step is split into two levels. In the first level, a modified set of momentum equations are solved for an auxiliary velocity field. The modification to the momentum equations is made by removing the pressure gradient. All that remains is to solve for the pressure which will map the auxiliary velocity into a divergence-free field. For this Chorin produces two equations, one in which the new velocity is calculated from the auxiliary velocity minus the pressure gradient, and in the second equation the change of pressure is calculated from the divergence of the new velocity. These have the dimensionless form

$$u_i^{n+1} = u_i^{aux} - \Delta t \frac{\partial}{\partial x_i} p^{n+1} \quad (1.1)$$

$$p^{n+1} = p^n - \lambda \text{Div}(u^{n+1}) \quad (1.2)$$

where  $\lambda$  is a constant chosen to facilitate convergence. These can be solved by iteration and result in a divergence-free flow field. By substituting equation (1.1) into equation (1.2) it is seen that this is equivalent to solving the Poisson equation in pressure

$$\nabla^2 p = \frac{1}{\Delta t} \text{Div}(u^{aux}) \quad (1.3)$$

If the convective and viscous terms from which the auxiliary field was computed were substituted into equation (1.3) then the resulting Poisson equation would be that of the previous method. So it can be seen that by performing the decomposition of the momentum equations and by computing the auxiliary field first results in a savings in the required number of floating point operations in each iteration. This method has been used by Kim and Moin (ref. 21) with some success to write a three-dimensional code in Cartesian coordinates which solves the Poisson equation in equation

(1.3) with a direct method. However, it is still preferable to avoid solving a Poisson equation in three-dimensional curvilinear coordinates as this would take more computing time than is desired.

To avoid the solution of a Poisson equation in pressure, there is the artificial compressibility method as first developed by Chorin (ref. 22). In this method, a time derivative of pressure is added to the continuity equation

$$\frac{\partial p}{\partial t} + \beta \frac{\partial u_i}{\partial x_i} = 0 \quad (1.4)$$

Together with the momentum equations this forms a hyperbolic-type system of equations. The equations can then be simultaneously advanced in time using a suitable algorithm. As the solution converges, the time derivative of pressure approaches zero and continuity is satisfied in the steady state. The artificial compressibility introduces pressure waves of finite speed into the incompressible flow, whose speed of sound would otherwise be infinite. These waves die out as the steady state is reached. This method was combined by Steger and Kurler (ref. 23) with an implicit approximate factorization scheme of Beam and Warming (ref. 24) for the computation of vortex wakes. This combination is known as the method of pseudocompressibility and is found to be computationally efficient. Because the continuity equation is not satisfied until the solution is converged to a steady state, this method is not time-accurate. But by temporarily relaxing the requirement of continuity, the steady state solution can be obtained at a significant savings in computing time. The use of this method currently appears to be the most viable approach to obtain incompressible steady state solutions for a complex three-dimensional geometry.

Pseudocompressibility was chosen by Kwak et al (refs. 25-26) in developing an efficient and robust code called INS3D, a three-dimensional, incompressible viscous flow solver in generalized curvilinear coordinates. This code was the main tool used in this research in an effort to study the best method for solving the incompressible Navier-Stokes equations.

The outline of this papers is given below. In the second section, the governing equations will be presented. The finite-difference algorithm will be described in the third section and the method of pseudocompressibility will be discussed further in the fourth section. Computed results will be presented in the fifth section for several test problems. These include a two-dimensional backward-facing step, flow behind a two-dimensional circular cylinder, and the flow around a cylinder-plate junction.

## GOVERNING EQUATIONS

### Incompressible Navier-Stokes Equations

The equations governing unsteady, three-dimensional, incompressible flow with constant density are presented. In these equations  $t$  is time;  $x$ ,  $y$ , and  $z$  are the Cartesian coordinates;  $u$ ,  $v$ , and  $w$  are the corresponding velocity components;  $p$  is the pressure; and  $\tau_{ij}$  is the viscous stress tensor. The equations have been written in dimensionless form using the following dimensionless variables

$$\begin{aligned} \tilde{u} &= \frac{u}{u_{ref}}, \tilde{v} = \frac{v}{u_{ref}}, \tilde{w} = \frac{w}{u_{ref}} \\ \tilde{x} &= \frac{x}{x_{ref}}, \tilde{y} = \frac{y}{x_{ref}}, \tilde{z} = \frac{z}{x_{ref}} \\ \tilde{t} &= \frac{tu_{ref}}{x_{ref}}, \tilde{p} = \frac{p - p_{ref}}{\rho u_{ref}^2}, \tilde{\tau}_{ij} = \frac{\tau_{ij}}{\rho u_{ref}^2} \\ \tilde{\nu} &= Re^{-1} = \frac{\nu}{x_{ref} u_{ref}}, \tilde{\beta} = \frac{\beta}{\rho u_{ref}^2} \end{aligned} \quad (2.1)$$

The subscript *ref* denotes reference quantities and in the following equations the tildes ( $\sim$ ) have been dropped for convenience.

The momentum equations are given by

$$\frac{\partial}{\partial t} \hat{q} + \frac{\partial}{\partial x} (\hat{e} - \hat{e}_v) + \frac{\partial}{\partial y} (\hat{f} - \hat{f}_v) + \frac{\partial}{\partial z} (\hat{g} - \hat{g}_v) = 0 \quad (2.2)$$

and the continuity equation is

$$\frac{\partial u}{\partial x} + \frac{\partial v}{\partial y} + \frac{\partial w}{\partial z} = 0 \quad (2.3)$$

where

$$\begin{aligned} \hat{q} &= \begin{bmatrix} u \\ v \\ w \end{bmatrix} \\ \hat{e} &= \begin{bmatrix} u^2 + p \\ uv \\ uw \end{bmatrix} \quad \hat{f} = \begin{bmatrix} vu \\ v^2 + p \\ vw \end{bmatrix} \quad \hat{g} = \begin{bmatrix} wu \\ wv \\ w^2 + p \end{bmatrix} \\ \hat{e}_v &= \begin{bmatrix} \tau_{xx} \\ \tau_{xy} \\ \tau_{xz} \end{bmatrix} \quad \hat{f}_v = \begin{bmatrix} \tau_{yx} \\ \tau_{yy} \\ \tau_{yz} \end{bmatrix} \quad \hat{g}_v = \begin{bmatrix} \tau_{zx} \\ \tau_{zy} \\ \tau_{zz} \end{bmatrix} \end{aligned} \quad (2.4)$$

To implement the pseudocompressibility scheme the continuity equation is replaced with

$$\frac{\partial p}{\partial t} + \beta \left( \frac{\partial u}{\partial x} + \frac{\partial v}{\partial y} + \frac{\partial w}{\partial z} \right) = 0 \quad (2.5)$$

Here  $\beta$  is the pseudo compressibility parameter which is chosen to facilitate fast convergence and will be discussed in more detail later.

Introducing Cartesian tensor notation, the viscous stress tensor can be written as

$$\tau_{ij} = 2\nu S_{ij} - R_{ij}. \quad (2.6)$$

Here,  $\nu$  is the kinematic viscosity,  $S_{ij}$  is the strain rate tensor, and  $R_{ij}$  is the Reynolds stress. These are given by

$$S_{ij} = \frac{1}{2} \left( \frac{\partial u_i}{\partial x_j} + \frac{\partial u_j}{\partial x_i} \right) \quad (2.7)$$

$$R_{ij} = \frac{1}{3} R_{kk} \delta_{ij} - 2\nu_t S_{ij}. \quad (2.8)$$

where  $u_i = u, v$ , or  $w$  for  $i = 1, 2$ , or  $3$ , respectively, and  $x_i = x, y$ , or  $z$  for  $i = 1, 2$ , or  $3$ , respectively. The normal component of the Reynolds stress is  $R_{kk}$  and  $\nu_t$  is the turbulent eddy viscosity. By substituting equations (2.7) and (2.8) into (2.6) and including the normal stress,  $R_{kk}$ , in the pressure, the viscous stress tensor becomes

$$\tau_{ij} = (\nu + \nu_t) \left( \frac{\partial u_i}{\partial x_j} + \frac{\partial u_j}{\partial x_i} \right). \quad (2.9)$$

In the remainder of this paper the total viscosity,  $(\nu + \nu_t)$ , will be represented simply by  $\nu$ .



By combining equations (2.2) and (2.5), the governing equations are written as one vector equation

$$\frac{\partial}{\partial t} D + \frac{\partial}{\partial x} (E - E_v) + \frac{\partial}{\partial y} (F - F_v) + \frac{\partial}{\partial z} (G - G_v) = 0 \quad (2.10)$$

where

$$\begin{aligned} D &= \begin{bmatrix} p \\ u \\ v \\ w \end{bmatrix} \\ E &= \begin{bmatrix} \beta u \\ u^2 + p \\ uv \\ uw \end{bmatrix} \quad F = \begin{bmatrix} \beta v \\ vu \\ v^2 + p \\ vw \end{bmatrix} \quad G = \begin{bmatrix} \beta w \\ wu \\ wv \\ w^2 + p \end{bmatrix} \\ E_v &= \begin{bmatrix} 0 \\ \tau_{xx} \\ \tau_{xy} \\ \tau_{xz} \end{bmatrix} \quad F_v = \begin{bmatrix} 0 \\ \tau_{yx} \\ \tau_{yy} \\ \tau_{yz} \end{bmatrix} \quad G_v = \begin{bmatrix} 0 \\ \tau_{zx} \\ \tau_{zy} \\ \tau_{zz} \end{bmatrix}. \end{aligned} \quad (2.11)$$

### Coordinate Transformation

To perform calculations on three-dimensional arbitrarily shaped geometries, the following generalized independent variables are introduced which transform the physical coordinates into general curvilinear coordinates

$$\begin{aligned} \tau &= t \\ \xi &= \xi(x, y, z, t) \\ \eta &= \eta(x, y, z, t) \\ \zeta &= \zeta(x, y, z, t) \end{aligned} \quad (2.12)$$

The spatial and time derivatives become

$$\begin{aligned} \frac{\partial}{\partial x_i} &= \frac{\partial \xi}{\partial x_i} \frac{\partial}{\partial \xi} + \frac{\partial \eta}{\partial x_i} \frac{\partial}{\partial \eta} + \frac{\partial \zeta}{\partial x_i} \frac{\partial}{\partial \zeta} = \frac{\partial \xi_j}{\partial x_i} \frac{\partial}{\partial \xi_j} \\ \frac{\partial}{\partial t} &= \frac{\partial}{\partial \tau} + \frac{\partial \xi_j}{\partial t} \frac{\partial}{\partial \xi_j} \end{aligned} \quad (2.13)$$

Here the Jacobian of the transformation is defined

$$J = \det \frac{\partial(\xi, \eta, \zeta)}{\partial(x, y, z)} = \begin{vmatrix} \xi_x & \xi_y & \xi_z \\ \eta_x & \eta_y & \eta_z \\ \zeta_x & \zeta_y & \zeta_z \end{vmatrix} \quad (2.14)$$

where

$$\xi_x = \frac{\partial \xi}{\partial x}, \quad \eta_y = \frac{\partial \eta}{\partial y}, \quad \text{etc.}$$

Before the transformation is applied, equation (2.10) is written

$$\frac{\partial}{\partial \tau} D + \frac{\partial}{\partial x_i} H_i = 0; \quad H_i = \begin{bmatrix} E - E_v \\ F - F_v \\ G - G_v \end{bmatrix} \quad (2.15)$$

Applying the transformation to this equation yields

$$\frac{\partial}{\partial t} D + \frac{\partial \xi_j}{\partial t} \frac{\partial}{\partial \xi_j} D + \frac{\partial \xi_j}{\partial x_i} \frac{\partial}{\partial \xi_j} H_i = 0 \quad (2.16)$$

After dividing through by the Jacobian, this can be decomposed into a conservative term and a remainder

$$\begin{aligned} & \frac{\partial}{\partial \tau} \left( \frac{D}{J} \right) + \frac{\partial}{\partial \xi_j} \left( \frac{D}{J} \frac{\partial \xi_j}{\partial t} + \frac{1}{J} \frac{\partial \xi_j}{\partial x_i} H_i \right) \\ &= D \frac{\partial}{\partial \tau} \left( \frac{1}{J} \right) + D \frac{\partial}{\partial \xi_j} \left( \frac{1}{J} \frac{\partial \xi_j}{\partial t} \right) + H_i \frac{\partial}{\partial \xi_j} \left( \frac{1}{J} \frac{\partial \xi_j}{\partial x_i} \right) \end{aligned} \quad (2.17)$$

It can be shown that the nonconservative remainder term on the right-hand side of equation (2.17) is equal to zero. Thus the governing equation, in an expanded form is

$$\begin{aligned} & \frac{\partial}{\partial \tau} \left( \frac{D}{J} \right) + \frac{\partial}{\partial \xi} \left\{ \frac{1}{J} [\xi_t D + \xi_x (E - E_v) + \xi_y (F - F_v) + \xi_z (G - G_v)] \right\} \\ &+ \frac{\partial}{\partial \eta} \left\{ \frac{1}{J} [\eta_t D + \eta_x (E - E_v) + \eta_y (F - F_v) + \eta_z (G - G_v)] \right\} \\ &+ \frac{\partial}{\partial \zeta} \left\{ \frac{1}{J} [\zeta_t D + \zeta_x (E - E_v) + \zeta_y (F - F_v) + \zeta_z (G - G_v)] \right\} \\ &= 0 \end{aligned} \quad (2.18)$$

This can be rewritten in the form

$$\frac{\partial \hat{D}}{\partial \tau} + \frac{\partial}{\partial \xi} (\hat{E} - \hat{E}_v) + \frac{\partial}{\partial \eta} (\hat{F} - \hat{F}_v) + \frac{\partial}{\partial \zeta} (\hat{G} - \hat{G}_v) = 0 \quad (2.19)$$

where

$$\begin{aligned} \hat{D} &= \frac{D}{J} \\ \hat{E} &= \frac{1}{J} [\xi_t D + \xi_x E + \xi_y F + \xi_z G] \\ &= \frac{1}{J} \begin{bmatrix} \xi_t p + \xi_x \beta u + \xi_y \beta v + \xi_z \beta w \\ \xi_t u + \xi_x (u^2 + p) + \xi_y v u + \xi_z w u \\ \xi_t v + \xi_x u v + \xi_y (v^2 + p) + \xi_z w v \\ \xi_t w + \xi_x u w + \xi_y v w + \xi_z (w^2 + p) \end{bmatrix} \end{aligned}$$

Now, the contravariant velocities,  $U$ ,  $V$ , and  $W$  without metric normalization are defined as

$$\begin{aligned} U &= \xi_t + \xi_x u + \xi_y v + \xi_z w \\ V &= \eta_t + \eta_x u + \eta_y v + \eta_z w \\ W &= \varsigma_t + \varsigma_x u + \varsigma_y v + \varsigma_z w. \end{aligned} \quad (2.20)$$

Using these,  $\hat{E}$ ,  $\hat{F}$ , and  $\hat{G}$  become

$$\begin{aligned} \hat{E} &= \frac{1}{J} \begin{bmatrix} \beta U + \xi_t(p - \beta) \\ uU + \xi_x p \\ vU + \xi_y p \\ wU + \xi_z p \end{bmatrix} \\ \hat{F} &= \frac{1}{J} \begin{bmatrix} \beta V + \eta_t(p - \beta) \\ uV + \eta_x p \\ vV + \eta_y p \\ wV + \eta_z p \end{bmatrix} \\ \hat{G} &= \frac{1}{J} \begin{bmatrix} \beta W + \varsigma_t(p - \beta) \\ uW + \varsigma_x p \\ vW + \varsigma_y p \\ wW + \varsigma_z p \end{bmatrix} \end{aligned} \quad (2.21)$$

The viscous terms are

$$\begin{aligned} \hat{E}_v &= \frac{1}{J} [\xi_x E_v + \xi_y F_v + \xi_z G_v] \\ \hat{F}_v &= \frac{1}{J} [\eta_x E_v + \eta_y F_v + \eta_z G_v] \\ \hat{G}_v &= \frac{1}{J} [\varsigma_x E_v + \varsigma_y F_v + \varsigma_z G_v] \end{aligned} \quad (2.22)$$

By using the values for  $E_v$  in equation (2.11),  $\hat{E}_v$  becomes

$$\hat{E}_v = \frac{1}{J} \begin{bmatrix} 0 \\ \xi_x \tau_{xx} + \xi_y \tau_{yx} + \xi_z \tau_{zx} \\ \eta_x \tau_{xy} + \eta_y \tau_{yy} + \eta_z \tau_{zy} \\ \varsigma_x \tau_{xz} + \varsigma_y \tau_{yz} + \varsigma_z \tau_{zz} \end{bmatrix} \quad (2.23)$$

Recalling equation (2.9) and applying the coordinate transformation to it, the shear stress tensor is

$$\tau_{ij} = \nu \left( \frac{\partial \xi_k}{\partial x_i} \frac{\partial u_j}{\partial \xi_k} + \frac{\partial \xi_k}{\partial x_j} \frac{\partial u_i}{\partial \xi_k} \right). \quad (2.24)$$

Substituting equation (2.24) into the equation for  $\hat{E}_v$  in (2.22) yields

$$\begin{aligned}\hat{E}_v &= \frac{\nu}{J} \left[ \begin{array}{c} 0 \\ \frac{\partial \xi}{\partial x_i} \frac{\partial \xi_k}{\partial x_i} \frac{\partial u}{\partial \xi_k} + \frac{\partial \xi}{\partial x_i} \frac{\partial \xi_k}{\partial x} \frac{\partial u_i}{\partial \xi_k} \\ \frac{\partial \eta}{\partial x_i} \frac{\partial \xi_k}{\partial x_i} \frac{\partial v}{\partial \xi_k} + \frac{\partial \eta}{\partial x_i} \frac{\partial \xi_k}{\partial y} \frac{\partial u_i}{\partial \xi_k} \\ \frac{\partial \zeta}{\partial x_i} \frac{\partial \xi_k}{\partial x_i} \frac{\partial w}{\partial \xi_k} + \frac{\partial \zeta}{\partial x_i} \frac{\partial \xi_k}{\partial z} \frac{\partial u_i}{\partial \xi_k} \end{array} \right] \\ \hat{E}_v &= \frac{\nu}{J} \left\{ \left[ \nabla \xi \cdot \nabla \xi \frac{\partial}{\partial \xi} + \nabla \xi \cdot \nabla \eta \frac{\partial}{\partial \eta} + \nabla \eta \cdot \nabla \zeta \frac{\partial}{\partial \zeta} \right] ImD \right. \\ &\quad \left. + \left( \xi_x \frac{\partial u}{\partial \xi_i} + \xi_y \frac{\partial v}{\partial \xi_i} + \xi_z \frac{\partial w}{\partial \xi_i} \right) \left[ \begin{array}{c} 0 \\ \frac{\partial}{\partial x} \xi_i \\ \frac{\partial}{\partial y} \xi_i \\ \frac{\partial}{\partial z} \xi_i \end{array} \right] \right\} \quad (2.25)\end{aligned}$$

where

$$Im = \begin{bmatrix} 0 & 0 & 0 & 0 \\ 0 & 1 & 0 & 0 \\ 0 & 0 & 1 & 0 \\ 0 & 0 & 0 & 1 \end{bmatrix}$$

If an orthogonal coordinate system is assumed, then

$$\nabla \xi_i \cdot \nabla \xi_j = 0; \text{ for } i \neq j$$

Then all the viscous terms become

$$\begin{aligned}\hat{E}_v &= \frac{\nu}{J} \left\{ \left( \xi_x^2 + \xi_y^2 + \xi_z^2 \right) Im \frac{\partial D}{\partial \xi} + \left( \xi_x \frac{\partial u}{\partial \xi_i} + \xi_y \frac{\partial v}{\partial \xi_i} + \xi_z \frac{\partial w}{\partial \xi_i} \right) \left[ \begin{array}{c} 0 \\ \frac{\partial}{\partial x} \xi_i \\ \frac{\partial}{\partial y} \xi_i \\ \frac{\partial}{\partial z} \xi_i \end{array} \right] \right\} \\ \hat{F}_v &= \frac{\nu}{J} \left\{ \left( \eta_x^2 + \eta_y^2 + \eta_z^2 \right) Im \frac{\partial D}{\partial \eta} + \left( \eta_x \frac{\partial u}{\partial \xi_i} + \eta_y \frac{\partial v}{\partial \xi_i} + \eta_z \frac{\partial w}{\partial \xi_i} \right) \left[ \begin{array}{c} 0 \\ \frac{\partial}{\partial x} \xi_i \\ \frac{\partial}{\partial y} \xi_i \\ \frac{\partial}{\partial z} \xi_i \end{array} \right] \right\} \\ \hat{G}_v &= \frac{\nu}{J} \left\{ \left( \zeta_x^2 + \zeta_y^2 + \zeta_z^2 \right) Im \frac{\partial D}{\partial \zeta} + \left( \zeta_x \frac{\partial u}{\partial \xi_i} + \zeta_y \frac{\partial v}{\partial \xi_i} + \zeta_z \frac{\partial w}{\partial \xi_i} \right) \left[ \begin{array}{c} 0 \\ \frac{\partial}{\partial x} \xi_i \\ \frac{\partial}{\partial y} \xi_i \\ \frac{\partial}{\partial z} \xi_i \end{array} \right] \right\} \quad (2.26)\end{aligned}$$

For constant  $\nu$  (i.e., laminar flow), the contribution by the second term in parathensis in the above equation will approach zero as the steady state is reached and equation (2.3) is numerically satisfied.

## NUMERICAL ALGORITHM

### Time-Advancing

The numerical algorithm used to advance equation (2.19) in time is an implicit, noniterative, approximately factored, finite-difference scheme by Beam and Warming (ref. 24). The time-differencing used by this scheme is generally known as the trapezoidal rule and is given by

$$\hat{D}^{n+1} = \hat{D}^n + \frac{\Delta\tau}{2} \left[ \left( \frac{\partial \hat{D}}{\partial \tau} \right)^n + \left( \frac{\partial \hat{D}}{\partial \tau} \right)^{n+1} \right] + O(\Delta\tau^3) \quad (3.1)$$

where the superscript  $n$  refers to the  $n^{\text{th}}$  time-step. The finite-difference form of equation (2.19) is

$$\delta_\tau \hat{D} + \delta_\xi (\hat{E} - \hat{E}_v) + \delta_\eta (\hat{F} - \hat{F}_v) + \delta_\zeta (\hat{G} - \hat{G}_v) = 0 \quad (3.2)$$

where  $\delta_\xi$  is the finite difference operator for  $\frac{\partial}{\partial \xi}$ , for example.  $\hat{E}$ ,  $\hat{F}$ , and  $\hat{G}$  are given by equation (2.21) and  $\hat{E}_v$ ,  $\hat{F}_v$ , and  $\hat{G}_v$  are given by equation (2.26). By substituting equation (3.2) into equation (3.1) and using  $D = \hat{D}J$ , one obtains

$$\begin{aligned} D^{n+1} + \frac{\Delta\tau}{2} J^{n+1} [\delta_\xi (\hat{E} - \hat{E}_v)^{n+1} + \delta_\eta (\hat{F} - \hat{F}_v)^{n+1} + \delta_\zeta (\hat{G} - \hat{G}_v)^{n+1}] \\ = \frac{J^{n+1} D^n}{J^n} - \frac{\Delta\tau}{2} J^{n+1} [\delta_\xi (\hat{E} - \hat{E}_v)^n + \delta_\eta (\hat{F} - \hat{F}_v)^n + \delta_\zeta (\hat{G} - \hat{G}_v)^n] \end{aligned} \quad (3.3)$$

The problem is to solve for  $D^{n+1}$ , and this is nonlinear in nature since  $\hat{E}^{n+1} = \hat{E}(D^{n+1})$  is a nonlinear function of  $D^{n+1}$  as are  $\hat{F}^{n+1}$  and  $\hat{G}^{n+1}$ . The following linearization procedure is used. A local Taylor expansion about  $u^n$  yields

$$\begin{aligned} \hat{E}^{n+1} &= \hat{E}^n + \hat{A}^n (D^{n+1} - D^n) + O(\Delta\tau^2) \\ \hat{F}^{n+1} &= \hat{F}^n + \hat{B}^n (D^{n+1} - D^n) + O(\Delta\tau^2) \\ \hat{G}^{n+1} &= \hat{G}^n + \hat{C}^n (D^{n+1} - D^n) + O(\Delta\tau^2) \end{aligned} \quad (3.4)$$

where  $\hat{A}$ ,  $\hat{B}$ , and  $\hat{C}$  are the Jacobian matrices

$$\hat{A} = \frac{\partial \hat{E}}{\partial D}, \quad \hat{B} = \frac{\partial \hat{F}}{\partial D}, \quad \hat{C} = \frac{\partial \hat{G}}{\partial D} \quad (3.5)$$

To evaluate these, recall that

$$D = \begin{bmatrix} p \\ u \\ v \\ w \end{bmatrix}$$

$$\hat{E} = \frac{1}{J} \left\{ \xi_t \begin{bmatrix} p \\ u \\ v \\ w \end{bmatrix} + \xi_x \begin{bmatrix} \beta u \\ u^2 + p \\ uv \\ uw \end{bmatrix} + \xi_y \begin{bmatrix} \beta v \\ vu \\ v^2 + p \\ vw \end{bmatrix} + \xi_z \begin{bmatrix} \beta w \\ wu \\ wv \\ w^2 + p \end{bmatrix} \right\}$$

Then

$$\hat{A} = \frac{1}{J} \begin{bmatrix} \xi_t & \xi_x \beta & \xi_y \beta & \xi_z \beta \\ \xi_x & U + \xi_x u & \xi_y u & \xi_z u \\ \xi_y & \xi_x v & U + \xi_y v & \xi_z v \\ \xi_z & \xi_x w & \xi_y w & U + \xi_z w \end{bmatrix} \quad (3.6)$$

where

$$U = \xi_t + \xi_x u + \xi_y v + \xi_z w$$

$\hat{B}$  and  $\hat{C}$  are obtained in a similar manner, and all three can be represented by the following, where  $\hat{A}_i = \hat{A}, \hat{B}, \text{ or } \hat{C}$  for  $i = 1, 2, \text{ or } 3$ , respectively.

$$\hat{A}_i = \frac{1}{J} \begin{bmatrix} L_0 & L_1 \beta & L_2 \beta & L_3 \beta \\ L_1 & Q + L_1 u & L_2 u & L_3 u \\ L_2 & L_1 v & Q + L_2 v & L_3 v \\ L_3 & L_1 w & L_2 w & Q + L_3 w \end{bmatrix} \quad (3.7)$$

where

$$Q = L_0 + L_1 u + L_2 v + L_3 w \\ L_0 = (\xi_i)_t, \quad L_1 = (\xi_i)_x, \quad L_2 = (\xi_i)_y, \quad L_3 = (\xi_i)_z$$

Substituting equation (3.4) into equation (3.3) results in the governing equation in delta form

$$\begin{aligned} & \left\{ I + \frac{\Delta \tau}{2} J^{n+1} \left[ \delta_\xi (\hat{A}^n - \Gamma_1) + \delta_\eta (\hat{B}^n - \Gamma_2) + \delta_\zeta (\hat{C}^n - \Gamma_3) \right] \right\} (D^{n+1} - D^n) \\ &= -\Delta \tau J^{n+1} \left[ \delta_\xi (\hat{E} - \hat{E}_v)^n + \delta_\eta (\hat{F} - \hat{F}_v)^n + \delta_\zeta (\hat{G} - \hat{G}_v)^n \right] \\ &+ \left( \frac{J^{n+1}}{J^n} - 1 \right) D^n \end{aligned} \quad (3.8)$$

where

$$\Gamma_1 D^{n+1} = \hat{E}_v^{n+1}, \quad \Gamma_2 D^{n+1} = \hat{F}_v^{n+1}, \quad \Gamma_3 D^{n+1} = \hat{G}_v^{n+1}$$

At this point it should be noted that the notation of the form  $[\delta_\xi (A - \Gamma)]D$  refers to  $\frac{\partial}{\partial \xi}(AD) - \frac{\partial}{\partial \xi}(\Gamma D)$  and not  $\frac{\partial A}{\partial \xi}D - \frac{\partial \Gamma}{\partial \xi}D$ .

### Approximate Factorization

The solution of equation (3.8) would involve a formidable matrix inversion problem. With the use of an ADI (alternating direction implicit) type scheme, the problem could be reduced to the inversion of three matrices of small bandwidth, for which there exist some efficient solution algorithms. The particular ADI form used here is known as approximate factorization (ref. 24). Using this, the governing equation becomes

$$L_\xi L_\eta L_\zeta (D^{n+1} - D^n) = RHS \quad (3.9)$$

where

$$\begin{aligned} L_\xi &= \left[ I + \frac{\Delta\tau}{2} J^{n+1} \delta_\xi (\hat{A}^n - \Gamma_1) \right] \\ L_\eta &= \left[ I + \frac{\Delta\tau}{2} J^{n+1} \delta_\eta (\hat{B}^n - \Gamma_1) \right] \\ L_\zeta &= \left[ I + \frac{\Delta\tau}{2} J^{n+1} \delta_\zeta (\hat{C}^n - \Gamma_1) \right] \end{aligned} \quad (3.10)$$

and  $RHS$  is the right-hand side of equation (3.8). When second-order central differencing is used, the solution to this problem becomes the inversion of three block tridiagonal matrices. The solution procedure is to solve these three problems

$$\begin{aligned} (L_\eta) \Delta \bar{D} &= RHS \\ (L_\xi) \Delta \bar{\bar{D}} &= \Delta \bar{D} \\ (L_\zeta) \Delta D^{n+1} &= \Delta \bar{\bar{D}}. \end{aligned} \quad (3.11)$$

As an example of one of the inversions, the procedure is illustrated for the  $\zeta$ -sweep, when  $(I + \frac{1}{2} \Delta\tau J^{n+1} \delta_\zeta C) \Delta D = \Delta \bar{\bar{D}}$  is solved for  $\Delta D$ , and  $C = \hat{C}^n - \Gamma_3$ . The computational domain indices used are  $j, k$ , and  $l$  for the  $\xi, \eta$ , and  $\zeta$  directions, respectively. Then using an LU decomposition, the following matrix equation is solved once for each  $j = 1$  to  $jmax$  and  $k = 1$  to  $kmax$ .

$$\begin{aligned} &\begin{bmatrix} I & 0 & 0 & 0 & \dots & 0 \\ -\tilde{C}_{j,k,1} & I & \tilde{C}_{j,k,3} & 0 & \dots & 0 \\ 0 & -\tilde{C}_{j,k,2} & I & \tilde{C}_{j,k,4} & \dots & 0 \\ \vdots & & & \ddots & & \vdots \\ 0 & \dots & 0 & \tilde{C}_{j,k,lmax-2} & I & \tilde{C}_{j,k,lmax} \\ 0 & \dots & 0 & 0 & 0 & I \end{bmatrix} \begin{bmatrix} \Delta D_{j,k,1} \\ \Delta D_{j,k,2} \\ \Delta D_{j,k,3} \\ \vdots \\ \vdots \\ \Delta D_{j,k,lmax} \end{bmatrix} \\ &= \begin{bmatrix} 0 \\ \Delta \bar{\bar{D}}_{j,k,2} \\ \Delta \bar{\bar{D}}_{j,k,3} \\ \vdots \\ \Delta \bar{\bar{D}}_{j,k,lmax-1} \\ 0 \end{bmatrix} \end{aligned} \quad (3.12)$$

where

$$\tilde{C} = \frac{1}{4} \Delta\tau J^{n+1} (\hat{C}^n - \Gamma_3)$$

$\hat{C}$  is given by equation (3.7) with  $i = 3$ , and  $\Gamma_3$  is given by equation (3.15).

Using this implementation, there will be no change in the variables at the boundaries, and the boundary conditions can be implemented explicitly. It is possible, however, to implement the boundary conditions implicitly, and this will be discussed in a later section.

The factorization has introduced the following second-order cross product term into the equation:

$$h^2 [\delta_\xi A \delta_\eta B + \delta_\eta B \delta_\zeta C + \delta_\zeta C \delta_\xi A] \Delta D + O(h^3) \quad (3.13)$$

where

$$A = \hat{A}^n - \Gamma_1, \quad B = \hat{B}^n - \Gamma_2, \quad C = \hat{C}^n - \Gamma_3, \quad h = \frac{\Delta\tau}{2} J^{n+1}$$

To maintain the second order accuracy of the scheme, the added terms must be kept smaller than the original terms in the equations everywhere in the computational domain. This puts a restriction on the size of the artificial compressibility parameter  $\beta$ . The proper choice of  $\beta$  will be discussed in a later section. In applying the approximate factorization scheme, it has been found that the stability of the scheme is dependent on the use of some higher-order smoothing terms. These are used to damp out higher frequency oscillations which arise in the solution because of the use of second-order central differencing, and will be discussed in the following section.

### Higher-Order Smoothing

Higher-order smoothing terms are required to make the present algorithm stable. These terms help to damp out the higher order oscillations in the solution that are caused by the use of second-order central differencing. The smoothing term is derived in conjunction with an upwind finite-difference approximation to  $\frac{\partial u}{\partial x}$  which is given as

$$\nabla_x u = \begin{cases} \frac{(3u_j - 4u_{j-1} + u_{j-2})}{2\Delta x} & \text{for } u > 0 \\ \frac{(-3u_j + 4u_{j+1} - u_{j+2})}{2\Delta x} & \text{for } u < 0 \end{cases} \quad (3.14)$$

where  $u_j = u(j\Delta x)$ . This equation can be written, for all  $u$

$$\begin{aligned} \nabla_x u &= \frac{1}{4\Delta x} [(3u_j - 4u_{j-1} + u_{j-2}) + (-3u_j + 4u_{j+1} - u_{j+2})] \\ &\quad + \frac{u}{4|u|\Delta x} [(3u_j - 4u_{j-1} + u_{j-2}) - (-3u_j + 4u_{j+1} - u_{j+2})] \end{aligned} \quad (3.15)$$

Replacing the first  $| |$  term of the above equation by a central difference formula results in

$$\nabla_x u = \frac{1}{2\Delta x} (u_{j+1} - u_{j-1}) + \frac{u}{4|u|\Delta x} (u_{j-2} - 4u_{j-1} + 6u_j - 4u_{j+1} + u_{j+2}). \quad (3.16)$$

This suggests that the proper form of the higher-order smoothing term should be that of the second term on the right-hand side of equation (3.16). This fourth-order term is represented using first-order upwind and downwind finite-difference operators

$$(\nabla_x \Delta_x)^2 u = \frac{1}{4\Delta x} (u_{j-2} - 4u_{j-1} + 6u_j - 4u_{j+1} + u_{j+2}) \quad (3.17)$$

Similarly, by starting with a first-order upwind equation, a second-order smoothing term can be derived

$$\nabla_x \Delta_x u = \frac{1}{2\Delta x} (u_{j+1} - 2u_j + u_{j-1}) \quad (3.18)$$

To compare how a small perturbation  $u'$  would act under the influence of each of these smoothing terms the following equation is used. Moving with the fluid, the perturbation under second-order smoothing is given by

$$\frac{\partial u'}{\partial t} - \epsilon \frac{\partial^2 u'}{\partial x^2} = 0$$



whose solution is

$$u' = e^{-\epsilon\alpha^2 t}(ae^{i\alpha x} + be^{-i\alpha x})$$

Under forth-order smoothing the perturbation is governed by

$$\frac{\partial u'}{\partial t} + \epsilon \frac{\partial^4 u'}{\partial x^4} = 0$$

whose solution is

$$u' = e^{-\epsilon\alpha^4 t}(ae^{i\alpha x} + be^{-i\alpha x})$$

Under the second-order smoothing, the lower frequency perturbations ( $\alpha < 1$ ) will be damped out faster than they will be with the fourth-order smoothing. For higher-frequency perturbations, the fourth-order smoothing will be more effective in damping the perturbation.

To preserve the tridiagonal nature of the system, only second-order smoothing is used on the left-hand side of the equation, and fourth-order smoothing is used on the right-hand side. The equation to be solved now becomes

$$\begin{aligned} & \left[ I + h\delta_\xi(\hat{A}^n - \Gamma_1) + \epsilon_i \nabla_\xi \Delta_\xi \right] \\ & \left[ I + h\delta_\eta(\hat{B}^n - \Gamma_2) + \epsilon_i \nabla_\eta \Delta_\eta \right] \\ & \left[ I + h\delta_\zeta(\hat{C}^n - \Gamma_3) + \epsilon_i \nabla_\zeta \Delta_\zeta \right] (D^{n+1} - D^n) \\ & = RHS - \epsilon_e \left[ (\nabla_\xi \Delta_\xi)^2 + (\nabla_\eta \Delta_\eta)^2 + (\nabla_\zeta \Delta_\zeta)^2 \right] D^n \end{aligned} \quad (3.19)$$

where  $\epsilon_i$  and  $\epsilon_e$  are implicit and explicit smoothing parameters. There is a good discussion on the characteristics of these parameters by Chang et al (ref. 27). For this analysis they assumed a perturbation  $p'$  given by

$$p'(\xi, \tau) = f(\tau)e^{i\alpha\xi}$$

where  $\xi$  is the free-stream direction. It was found that in order to damp out the numerical fluctuations as time advances, the smoothing parameters must satisfy

$$\epsilon_i > \epsilon_e \left( \frac{\alpha^2}{2} \right) \quad (3.20)$$

Employing discrete Fourier analysis, a necessary condition on these coefficients can be derived, namely

$$\epsilon_i > 2\epsilon_e \quad (3.21)$$

However, the exact relation between these two coefficients can only be determined by a nonlinear stability analysis. For the results given in this paper,  $\epsilon_i$  is taken to be 0.3 and  $\epsilon_e$  is 0.1 for the smoothing on the velocity components. For the smoothing on the pressure, larger values are usually used. This will be discussed further in a following section.

### Boundary Conditions

An important part of any computer code is the proper implementation of boundary conditions. The code must be capable of handling the several different types of boundaries encountered in numerical simulations which include solid surface, in-flow and out-flow, and far-field boundaries.

## Solid Surface

At a solid surface boundary, the usual no-slip condition is applied. In general the grid point adjacent to the surface will be sufficiently fine so that constant pressure normal to the surface in the viscous boundary layer can be assumed. For a  $\zeta = \text{constant}$  surface, this can be expressed as

$$\left( \frac{\partial p}{\partial \zeta} \right)_{L=1} = 0. \quad (3.22)$$

This boundary condition can be implemented either explicitly or implicitly. The explicit implementation uses equation (3.12) for the matrix inversion and then the pressure on the boundary can be computed at the end of the time-step using a suitable finite-difference form of equation (3.22). The implicit implementation, however, will enhance the stability of the code. This can be done during the  $\zeta$  sweep by replacing the first row of the matrix equation (3.12) with

$$I\Delta D_{j,k,1} + \hat{c}\Delta D_{j,k,2} = \hat{f} \quad (3.23)$$

where

$$\hat{c} = \begin{bmatrix} -1 & 0 & 0 & 0 \\ 0 & 0 & 0 & 0 \\ 0 & 0 & 0 & 0 \\ 0 & 0 & 0 & 0 \end{bmatrix} \quad \hat{f} = \begin{bmatrix} p_{L=2} - p_{L=1} \\ 0 \\ 0 \\ 0 \end{bmatrix}$$

## In-flow, Out-flow and Far-field Conditions

The in-flow and out-flow boundary conditions for an internal flow problem and the far-field boundary conditions for an external flow problem can be handled in much the same way. The incoming flow for both problems can be set to some appropriate constant as dictated by the problem. For example, at the inlet to a pipe, the pressure can be set to a constant and the velocity profile can be specified to be uniform. The conditions at the downstream however, are the most difficult to provide. Simple upwind extrapolation is not well-posed. The best convergence rate is obtained if global mass is conserved. So to ensure the best results, the velocities and pressure are first updated using a second-order upwind extrapolation. For an exit at  $L = l_{\max}$  this is

$$Q_{l_{\max}}^{\tilde{n}} = \frac{Q_{l_{\max}-1}^{n+1} \left( \frac{\Delta z_2}{\Delta z_1} \right) - Q_{l_{\max}-2}^{n+1}}{\frac{\Delta z_2}{\Delta z_1} - 1} \quad (3.24)$$

where

$$\Delta z_1 = z_{l_{\max}} - z_{l_{\max}-1}$$

$$\Delta z_2 = z_{l_{\max}} - z_{l_{\max}-2}$$

Then, these extrapolated velocities are integrated over the exit boundary to obtain the outlet mass flux

$$\dot{m}_{out} = \int_{exit} \vec{V}^{\tilde{n}} \cdot d\hat{a}. \quad (3.25)$$

Then the velocity components are weighted by the mass flux ratio to conserve global mass

$$\vec{V}^{n+1} = \frac{\dot{m}_{in}}{\dot{m}_{out}} \vec{V}^{\tilde{n}} \quad (3.26)$$

If nothing further is done to update the boundary pressure, this can lead to discontinuities in the pressure because momentum is not being conserved. A method of weighting the pressure by a momentum correction was presented by Chang et al (ref. 27). They use the following to obtain a pressure which corresponds to the mass weighted velocities

$$p^{n+1} = p^{\bar{n}} - \frac{1}{\zeta_z} [(wW)^{n+1} - (wW)^{\bar{n}}] + \frac{\nu}{\zeta_z} (\nabla \zeta \cdot \nabla \zeta) \left[ \left( \frac{\partial w}{\partial \zeta} \right)^{n+1} - \left( \frac{\partial w}{\partial \zeta} \right)^{\bar{n}} \right] \quad (3.27)$$

where  $W$  is the contravariant velocity given by Eq. (2.20). In obtaining this formula, it has been assumed that the streamlines near the exit plane are nearly straight. Any appreciable deviation will cause a discontinuity in the pressure and may lead to an instability. To avoid this, a momentum weighted pressure was used. This was obtained by integrating the momentum corrected pressure  $p^{n+1}$  and the extrapolated pressure  $p^{\bar{n}}$  across the exit

$$\begin{aligned} I_p^{n+1} &= \int_{exit} p^{n+1} d\hat{a} \\ I_p^{\bar{n}} &= \int_{exit} p^{\bar{n}} d\hat{a}. \end{aligned} \quad (3.28)$$

The final outlet pressure is then taken to be

$$p^{n+1} = \left( \frac{I_p^{n+1}}{I_p^{\bar{n}}} \right) p^{\bar{n}}. \quad (3.29)$$

Using these downstream boundary conditions global conservation of mass and momentum are ensured and the scheme will not introduce instabilities into the flow field.

## PSEUDOCOMPRESSIBILITY

In an incompressible flow, a disturbance in the pressure causes waves which travel with infinite speed. Introducing pseudocompressibility results in waves of finite speed, where the magnitude of the speed depends upon the pseudocompressibility constant  $\beta$ . In a true incompressible flow, the pressure field is affected instantaneously by a disturbance in the flow, but with pseudocompressibility, there will be a time lag between the flow disturbance and its effect on the pressure field. In viscous flows, the behavior of the boundary layer is very sensitive to the stream-wise pressure gradient, especially when the boundary layer is separated. If separation is present, a pressure wave traveling with finite speed will cause a change in the local pressure gradient which will affect the location of the flow separation. This change in separated flow will feed back to the pressure field, possibly preventing convergence to a steady state.

### Characteristics of The Pressure Wave

To analyze the behavior of this pressure wave and obtain the pseudo sound speed, a one-dimensional form of the governing equations is used

$$\begin{aligned}\frac{\partial p}{\partial t} + \beta \frac{\partial u}{\partial x} &= 0 \\ \frac{\partial u}{\partial t} + \frac{\partial u^2}{\partial x} &= -\frac{\partial p}{\partial x} - \tau_w\end{aligned}\tag{4.1}$$

where  $\tau_w$  is the normalized shear stress at the wall. For the purpose of finding the pseudo sound speed, the shear stress is neglected. If the sound speed is denoted as  $c$ , and  $x$  denotes the position of the pressure wave, then an upstream traveling wave is moving at a speed of  $c - u$ . During a short time interval  $\Delta t$ , the wave will travel a short distance  $\Delta x$ . As  $\Delta t$  approaches zero,

$$\frac{\partial x}{\partial t} = c - u$$

and

$$\begin{aligned}\frac{\partial u}{\partial t} &= \frac{\partial u}{\partial x} \frac{\partial x}{\partial t} = (c - u) \frac{\partial u}{\partial x} \\ \frac{\partial p}{\partial t} &= \frac{\partial p}{\partial x} \frac{\partial x}{\partial t} = (c - u) \frac{\partial p}{\partial x}\end{aligned}\tag{4.2}$$

Substituting this into equation (4.1) and solving for  $c$  leads to

$$c = \sqrt{u^2 + \beta}\tag{4.3}$$

The pseudo Mach number can be defined

$$M = \frac{u}{c} = \frac{u}{\sqrt{u^2 + \beta}}\tag{4.4}$$

which is always less than one for any  $\beta > 0$ . This is a necessary condition so that the pressure wave will propagate upstream and effect the whole flow field.

### Wave-Vorticity Interactions

In their paper, Chang and Kwak (ref. 28) presented an analysis of the interaction between the finite-speed pressure wave and the development of the boundary layer in order to set a theoretical lower limit for  $\beta$ . Their analysis is summarized here. The wave has to travel fast enough to allow proper distribution of the pressure while the boundary layer develops. In their analysis the following equations are obtained from equation (4.1) by linearizing the momentum flux locally, and cross differentiating

$$\begin{aligned}\frac{\partial^2 p}{\partial t^2} + 2\bar{U}_0 \frac{\partial^2 p}{\partial t \partial x} - \beta \frac{\partial^2 p}{\partial x^2} &= \beta \frac{\partial \tau_w}{\partial x} \\ \frac{\partial^2 u}{\partial t^2} + 2\bar{U}_0 \frac{\partial^2 u}{\partial t \partial x} - \beta \frac{\partial^2 u}{\partial x^2} &= -\frac{\partial \tau_w}{\partial t}\end{aligned}\tag{4.5}$$

which can be written as

$$\left[ \frac{\partial}{\partial t} + (\bar{U}_0 + c) \frac{\partial}{\partial x} \right] \left[ \frac{\partial}{\partial t} + (\bar{U}_0 - c) \frac{\partial}{\partial x} \right] \begin{pmatrix} p \\ u \end{pmatrix} = \begin{pmatrix} \beta \frac{\partial \tau_w}{\partial x} \\ -\frac{\partial \tau_w}{\partial t} \end{pmatrix}\tag{4.6}$$

where  $c$  is the pseudo sound speed in equation (4.3) and  $\bar{U}_0$  is the mean velocity in the primary flow direction.

If the right-hand side of equation (4.6) is neglected, the result would be the characteristic equations for two families of linear waves

$$\begin{aligned} \left[ \frac{\partial}{\partial t} + (u + c) \frac{\partial}{\partial x} \right] \begin{pmatrix} p^+ \\ u^+ \end{pmatrix} &= 0 \\ \left[ \frac{\partial}{\partial t} + (u - c) \frac{\partial}{\partial x} \right] \begin{pmatrix} p^- \\ u^- \end{pmatrix} &= 0 \end{aligned} \quad (4.7)$$

The (+) family of waves propagate downstream with a velocity of  $c + u$ , and the (-) family of waves propagate upstream with a velocity of  $c - u$ .

If the shear stress term is included, then there is a coupling between the pseudo pressure waves and the vorticity spreading since the shear stress depends on the velocity field. Since the upstream traveling waves travel more slowly, these will be studied. For these waves, the coupling may be described by

$$\frac{\partial u^-}{\partial t} + (u - c) \frac{\partial u^-}{\partial x} = - \frac{\partial \tau}{\partial t} \quad (4.8)$$

To investigate the coupling effect, the problem of a flow through a channel of width  $x_{ref}$  and length  $L$  is considered. The wave with the lowest wave number and therefore a length scale of  $L$  will be studied and so the following quantities will be used

$$\tilde{x} = \frac{x}{L}, \quad \tilde{t} = \frac{(u - c)t}{L}, \quad t_\nu = \frac{4}{Re}t$$

The rate of vorticity spreading for laminar flow is approximately given by

$$\frac{d\delta^2}{dt} \approx \frac{4}{Re} \quad (4.9)$$

The scaled variable  $t_\nu$  was chosen such that

$$\frac{d\delta^2}{dt_\nu} \approx 1$$

Using these variables, equation (4.8) becomes

$$\frac{\partial u^-}{\partial \tilde{t}} + \frac{\partial u^-}{\partial \tilde{x}} = - \left[ \frac{4L}{Re(u - c)} \right] \frac{\partial \tau_w}{\partial t_\nu} \quad (4.10)$$

where  $\tau_w = \tau_w(u, \delta(t_\nu))$ . In this equation, the two  $u^-$  partial derivative terms are of order 1 and the shear stress partial derivative term is of the order of 1 or less, depending on the size of the boundary layer. Therefore, the interactions between the waves and the vorticity can be decoupled if the coefficient on the right-hand side of equation (4.10) is very small

$$\left[ \frac{4L}{Re(u - c)} \right] \ll 1 \quad (4.11)$$

By plugging the expression for the pseudo sound speed into this equation and assuming the normalized velocity of the primary flow  $u$  to be unity, the restriction for  $\beta$  is obtained

$$\beta \gg \left(1 + \frac{4L}{Re}\right)^2 - 1 \quad (4.12)$$

The physical meaning of this restriction can be thought of as follows. The time it takes an upstream wave to travel the distance of the computational domain of length  $L$  is

$$T_L = \frac{L}{c - u} \quad (4.13)$$

Using equation (4.9), the time required for vorticity to spread a thickness  $\delta$  is approximately

$$T_\delta \approx \frac{Re}{4} \delta^2 \quad (4.14)$$

If it is required that the pressure wave travel the full length of the computational domain before the viscosity has diffused through the flow, then

$$T_L < T_\delta \quad (4.15)$$

By substituting in equations (4.13) and (4.14) into equation (4.15) and taking  $\delta = x_{ref} = 1$ , the restriction in equation (4.11) is obtained.

This analysis provides a lower bound for the choice of  $\beta$ . For the upper bound of  $\beta$ , the error introduced by the approximate factorization will be considered. Recalling equation (3.13), the form of the error is

$$E = \left(\frac{\Delta\tau}{2} J^{n+1}\right)^2 \left[ \delta_\epsilon (\hat{A}^n - \Gamma_1) \delta_\eta (\hat{B}^n - \Gamma) + \dots \right] \quad (4.16)$$

This term must be kept smaller than the original terms in the equation. Including only the terms which contain  $\beta$ , this restriction can be expressed as

$$\frac{\Delta\tau}{2} J^{n+1} \delta_{\epsilon_i} \hat{A}_i^n \delta_{\epsilon_j} \hat{A}_j^n < \delta_{\epsilon_i} \hat{A}_i^n, \quad i \neq j$$

or

$$\frac{\Delta\tau}{2} J^{n+1} \delta_{\epsilon_j} \hat{A}_j^n < 1 \quad (4.17)$$

Recalling the expression for  $\hat{A}_i^n$  given by equation (3.7), the terms which have  $\beta$  in them give the following

$$\frac{\Delta\tau}{2} \beta \delta_{\epsilon_j} \left( \frac{\partial \xi_j}{\partial x_i} \right) < 1 \quad (4.18)$$

The term to the right of  $\beta$  in this inequality is essentially the change in  $\frac{1}{\Delta x_i}$  in either the  $\xi$ ,  $\eta$ , or  $\zeta$  direction. An estimate of the order of magnitude of this term for the grids used in this study is given by

$$O \left[ \delta_{\epsilon_j} \left( \frac{\partial \xi_j}{\partial x_i} \right) \right] \approx 2 \quad (4.19)$$

which puts the restriction on  $\beta$

$$O(\beta \Delta \tau) < 1 \quad (4.20)$$

For most problems, the restrictions for  $\beta$  given by equations (4.12) and (4.20) are satisfied with a value for  $\beta$  in the range from 1 to 10.

To test the validity of these restrictions, a test problem was run over a range of  $\beta$ . The problem used was flow through a two-dimensional channel with a width of 1 and a length of 15. The prescribed inlet conditions were that of a uniform flow and a pressure of unity. The grid used, shown in figure 1, has 31 points in the cross-stream direction, and 65 points in the streamwise direction. The Reynolds number used is 1000 based on the duct width and inlet flow velocity; the time-step used in the calculations is  $\Delta \tau = 0.1$ .

For a proper convergence, the above equations for the restrictions on  $\beta$  give the following range

$$0.1236 < \beta < 10 \quad (4.21)$$

To test these values, the problem was run for the five values of  $\beta = 0.1, 1.0, 5.0, 10.0$ , and  $50.0$ . The solution converged only for the cases of  $\beta = 1.0, 5.0$ , and  $10.0$ . The converged velocity profiles are shown for the case of  $\beta = 5.0$  in figure 2.

The convergence history of the five cases is shown in figure 3. The log (base 10) of the root-mean-square of the change in flow variables is plotted versus the computational time  $\tau$ . It can be seen that the calculations for the cases of  $\beta = 0.1$  and  $50.0$  become unstable within 100 time steps and blow up, whereas the other cases converge to a stable solution. This indicates that the restrictions given in equations (4.12) and (4.20) are valid for this problem. In fact, these restrictions have proven to be valid for all cases yet encountered with this code. In figure 4, the effect of the various values of  $\beta$  on the incompressibility of the fluid is shown. The log of the root-mean-square of the divergence of the velocity field is plotted versus time. Again, the instability of the large and small  $\beta$  is seen, and the best convergence toward an incompressible solution is given with  $\beta = 5.0$ .

To illustrate the effect of the traveling pressure wave in the channel flow, the following pressure contours are shown for the cases of  $\beta = 0.1$  and  $\beta = 5.0$ . In figure 5, the contours are shown for  $\beta = 5.0$  at the computational times of 1.0, 2.5, and 4.0. The contours for  $\beta = 0.1$  are shown at the same times in figure 6. In both cases, it can be seen that the pressure is dropping at the exit as the downstream boundary condition enforces conservation of global mass. For the  $\beta = 5.0$  case, these contours propagate upstream as time progresses and the proper pressure drop begins to develop. For the  $\beta = 0.1$  case, however, the pressure gradient does not propagate upstream nearly as fast. For this case at  $\tau = 2.5$ , the pressure gradient remains large near the outlet, the contours are not spreading upstream. The solution becomes unstable and this is shown by the interesting pattern in the contours as the pressure develops discontinuities.

### Effects of Smoothing on Pressure

The explicit smoothing has a large effect on the convergence and accuracy of the pseudo-compressibility method. In particular, the explicit smoothing on the pressure can effect whether or not the solution converges to an incompressible flow field. In their paper, Chang and Kwak (ref. 28) showed that the pseudo pressure waves decay exponentially with time and vanish as the solution converges. Thus the change in pressure with time approaches zero. When there is no explicit smoothing added to the equation, as in equation (2.4), then the divergence of the velocity field identically approaches zero. However, when explicit smoothing is included, as the change in pressure approaches zero, the divergence of velocity approaches

$$\nabla \cdot \vec{V} \rightarrow -\frac{\epsilon_c(1)}{\beta} [(\nabla_\epsilon \Delta_\epsilon)^2 + (\nabla_\eta \Delta_\eta)^2 + (\nabla_\zeta \Delta_\zeta)^2] p \quad (4.22)$$

where  $\epsilon_c(1)$  is the explicit smoothing parameter for the pressure. When the pressure gradients become substantial, as in the case when a region of separation is present, the smoothing term does not approach zero and this contaminates the incompressibility of the solution.

To alleviate this problem, the value of  $\epsilon_c(1)$  is decreased with time. For the cases illustrated in the previous section,  $\epsilon_c(1)$  was decreased by half of its value at every 50 time steps, from a starting value of 0.12, which is why there are kinks in the convergence curves in figures 3 and 4. In this section, the same problem was used to illustrate the effect of the smoothing. For these cases, an exponentially decaying value of  $\epsilon_c(1)$  was used

$$\epsilon_c(1) = 1.0e^{-\alpha t} \quad (4.23)$$

for the values of  $\alpha = 0.01, 0.05, 0.1$ , and  $0.5$ . The results are presented in figures 7-10. Here, the logs of RMSDQ, RMSCO, and RMSDIV are plotted versus time, where RMSDQ is the root-mean-square of the change in the flow variables at every time step; where RMSCO is the root-mean-square of the right-hand side of the continuity equation, which includes the divergence of the velocity and the smoothing terms; and where RMSDIV is the root-mean-square of the divergence of the velocity field.

Since the right-hand side of the continuity equation is equal to

$$(-\beta \Delta \tau \text{div} \vec{V} - \text{smoothing terms})$$

then when  $\beta = 5$  and  $\Delta \tau = 0.1$  and as the smoothing dies out, it is expected that RMSDIV will approach 2·RMSCO. In figure 7, for the case of  $\alpha = 0.01$ , RMSCO rapidly converges but the divergence does not as it is being influenced heavily by the smoothing terms. In the next figures, it is seen that as the smoothing approaches zero, then the divergence of the velocity field converges at the same rate as RMSCO.

## COMPUTED RESULTS

To test the accuracy of the code, two test problems are used. It was desired that both an internal flow and an external flow be tested. The first test case is that of laminar flow through a two-dimensional backward-facing step, the second is laminar flow around a two-dimensional circular cylinder. Both of these cases have experimental data available for comparison, and both have regions of separated flow which will test the ability of pseudocompressibility to distribute the pressure in the presence of a shear layer without causing an instability. Since the cylinder flow is unstable for a Reynolds number greater than 40, the numerical solution will not converge and a pseudo unsteady behavior will be observed.

Finally, a flow that is highly three-dimensional in nature is studied. For this, the flow about a three-dimensional cylinder on a flat plate is used.

### Backward Facing Step

The flow over a backward-facing step was computed and the reattachment length was calculated for Reynolds numbers in the laminar range. The geometry of this problem is shown in figure 11. Here, the Reynolds number is based on twice the step height. The upstream boundary is located at the step and the inlet velocity profile there is prescribed to be a parabola (fully developed channel flow). The computations were conducted using a  $65 \times 33$  grid similar to that shown in figure 1. The results of the experiment performed by Armaly et al (ref. 29) were used as a comparison to judge the accuracy of the computations. They reported that the flow at the step showed only a very small deviation from a parabolic profile, so that the placement of the inlet at the step should not introduce a significant error.



In the initial calculations, the code severely underpredicted the separation length at the higher range of Reynolds numbers. However, because of the presence of the explicit smoothing term in equation (4.22), the steady-state solution was not approaching a divergence free state. After the explicit smoothing parameter for pressure was decreased with time, the following results were obtained. In figure 12, the separation length versus the Reynolds number for three different computational codes and the experiment are plotted.

INS3D shows remarkably good agreement with the experimental results for the full range of Reynolds numbers. The computations from the TEACH code were performed by Armaly et al (ref. 29) to coincide with their experimental results. The number of grid points they could use was limited by their computer's core memory, and they claim this could explain the discrepancy between their numerical results and the experimental results for the higher Reynolds numbers. The data from Kim and Moin (ref. 21) are the results of running their fractional step code with the same boundary conditions and number of grid points that were used to run INS3D. Their code uses an approximate factorization scheme and solves a Poisson equation for pressure using a direct method based on trigonometric expansions. They use a staggered grid and the code is written for a uniform Cartesian mesh.

In the INS3D calculations, opposite wall separation was present for Reynolds numbers of 500 and greater, which agrees with the results of the experiment. As in the case where the results were reported by the experiment, the opposite wall separation begins upstream from the reattachment point of the primary separation, and ends downstream from it. However, the magnitude of the computed opposite wall bubble is smaller than that found in the experiment. For the range of Reynolds numbers from 500 to 800, the length of this bubble was computed to be from 1 to 4 step-heights. The size in the experiment ranged from 5 to 8 step-heights in this range. Kim and Moin reported 7.8 step-heights for a Reynolds number of 600 and 11.5 step-heights for the 800 Reynolds number case.

To compare the efficiency of the fractional step code with the INS3D code, the computing times used to solve the backward-facing step problem are presented in table 1. The convergence criteria were equivalent for the two cases. The computations were performed on a Cray X/MP and the times are given in units of CPU seconds. The calculation times for the two codes are comparable, with INS3D being a little more efficient.

Table 1. COMPUTING TIME FOR BACKSTEP PROBLEM.

Reynolds Number	INS3D	Fractional Step
100	120	92
200	121	186
300	155	315
400	230	491
500	604	649
600	614	718
700	582	803
800	601	867

In the next two figures, the results of INS3D's calculations for a Reynolds number of 700 are shown. In figure 13, the streamlines are plotted, and in figure 14, velocity profiles at various points in the flow are shown.

## Circular Cylinder

The flow around a two-dimensional circular cylinder is rich in fluid physics. This flow is generally found to be steady for a Reynolds number less than 40 (ref. 30). Calculations for a Reynolds number of 40 have been carried out using INS3D and reported by Kwak et al (ref. 25). The quantities they reported include the wake length,  $L_{wake}$ ; the separation angle,  $\theta_{sep}$ ; the pressure drag,  $C_{dp}$ ; and the pressure coefficients at the forward and rear stagnation points,  $C_{pf}$  and  $C_{pr}$ . All these quantities were in good agreement with a summary of experimental results found in literature and are repeated in table 2 for reference.

Table 2: CIRCULAR CYLINDER FLOW AT  $Re = 40$ .

	Summary of literature	INS3D
$C_{dp}$	0.93–1.05	1.03
$C_{pf}$	1.14–1.23	1.15
$C_{pr}$	-0.47– -0.55	-0.51
$\theta_{sep}$	50°–53.9°	52°
$L_{wake}$	1.8–2.5	1.9

### Impulsively Started Symmetric Flow

The development of the symmetric wake for an impulsively started circular cylinder was computed. The 120 by 85 grid shown in figure 15 was used for these calculations. The flow visualization results compare well with that of an experiment. In figure 16, the wake behind an impulsively started cylinder at a Reynolds number of 1200 is shown at nondimensional times of 1.1, 1.3, 1.9, 2.4, 2.9, and 3.1 for both the experiment of Nagata et al (ref. 31) and the calculations of INS3D. The time-step used in the computations was 0.02. The similarity is striking, not only in the growth of the primary separation regions, but also in the appearances of two secondary bubbles near the point of separation.

Bouard and Contanceau (ref. 32) also presented experimental results for an impulsively started circular cylinder. For the range  $800 < Re < 5000$ , they noted what they call phenomenon  $\alpha$ . First, for  $\tau > 1$ , near the wall and about half-way between the stagnation and separation points a bulge appears forcing the streamlines out from the wall. They noted that this bulge develops into a little secondary eddy by  $\tau > 1.5$ . The very beginnings of this bulge can be seen in the computed streamlines at  $\tau = 1.3$ , and the secondary eddy is developed by  $\tau = 1.9$ . In the experiment they noted that the eddy grows to touch the outer boundary of the primary eddy, splitting off another small eddy from the primary eddy. This new eddy is equal in size and strength to the secondary eddy, thus there is a pair of secondary eddies formed. This can clearly be seen in the next three pictures of the computed streamlines. These same features have also been experimentally observed by Honji & Taneda (ref. 33), and Taneda (ref. 34), and numerically by Thoman & Szweczyk (ref. 35), and more recently by Loc (ref. 36), and Lecointe & Piquet (ref. 37).

### Vortex Shedding

Even though the present algorithm is designed for obtaining steady-state solutions, pseudo-unsteady characteristics are examined in this section. In order to observe periodic behavior in the wake of the cylinder, it was necessary to introduce a perturbation in the flow field. For

this, surface roughness equal to 2% of the diameter was applied to one side of the body. Once the periodic motion had started, no further disturbance was needed to continue to shedding, and a smooth grid was used for further calculations. The calculations were carried out at a Reynolds number of 1200, for which a Strouhal number in the range of 0.17 to 0.2 (ref. 30) has been found in experiment. Using a time-step of 0.01, the calculated Strouhal number varied from 0.357 to 0.303 depending on what mesh was used. The value of 0.303 was obtained on the finest mesh used, that being 140 by 120. The lift and coefficient of pressure drag versus time are shown in figures 17 and 18, respectively, starting at a time when the smooth grid was used. These are the calculations for the 120 by 85 grid and the Strouhal number based on the frequency of the pressure drag over this time interval is 0.357. Since the calculations never approach a steady state, the pseudo pressure waves never die out, and the calculated flow will not become completely divergence-free. For these calculations, the root mean square of the divergence of the velocity field had an average value of 0.02, so it is not surprising that the calculations did not predict the correct Strouhal number. However, the phenomenon of vortex shedding is qualitatively shown by this method of computation.

Streamlines at different times in the period are shown in figure 19 at times of 10.4, 11.1, 11.8, 12.5, and 13.3. At  $\tau = 10.4$ , both the lift and drag are at a maximum, and it can be seen that a vortex is about to be shed from the upper half of the cylinder. Here it can be seen that the core streamlines on the top surface fully encircle the separated region and travel all the way to the lower half before starting downstream. At the next time frame, the separated region has begun to open up, and the lift starts to drop but it is still positive. In the next frame, the lift is nearly zero, and the drag is at a minimum. In the next frame the lower separated region begins to form and the lift is becoming negative, while the drag begins to increase. In the last frame, the lift has just turned past the minimum, and the streamlines are almost a reversed image of the first frame.

### Three-Dimensional Calculations

The code INS3D has been used to calculate the flow for several different complex three-dimensional objects including a geometry used to model the Space Shuttle Main Engine (refs 25 and 27). As an example of the three-dimensional capability, the flow is calculated for the problem of two parallel plates with a cylinder normal to the plate surface attached between the two plates. This geometry is similar to a flow in the Space Shuttle Main Engine where hot hydrogen gas under high pressure is flowing around posts which carry liquid oxygen. Since the flow is symmetric about the center plane between the plates, only one plate with half the cylinder will be used in the calculations. The inflow is prescribed to be a parabolic profile, and the Reynolds number is based on the average inflow velocity and the diameter of the cylinder. The grid and inflow are shown in figure 20, with a close up of the grid spacing at the cylinder-plate junction shown in figure 21.

The solution to this problem was found to be steady, and some interesting features of the flow were found in the calculations. A saddle point of separation and a nodal point of reattachment appeared in front of the cylinder as shown in figures 22 and 23. Figure 22 is a top view of the velocity vectors in the  $z$  plane next to the wall at  $z/D = 0.02$ , where  $D$  is the diameter of the cylinder. The saddle point of separation appears at  $y/D = -2.9$ , and the nodal point of reattachment is at  $y/D = -0.56$ . Figure 23 is a side view of the velocity vectors in the plane at  $x/D = 0.0$ . Figure 24 shows particle traces of the computed flow for particles released on either side of the  $x/D = 0.0$  plane. Particles which are released near the region of the separated flow between the saddle point of separation and the nodal point of reattachment show the presence of a horseshoe vortex. Particles released between the nodal point of separation and the body show the existence of a pair of spiraling vortex filaments which wrap around the cylinder and spiral upward. This secondary vortex has a sense opposite that of the horseshoe vortex.

## CONCLUSION

An incompressible flow solver has been developed which is capable of computing the steady-state solution to a realistic three-dimensional geometry. Pseudocompressibility has been found to be an efficient way to solve the pressure field, and although this limits the time-accuracy, it is capable of showing the qualitative nature of an unsteady problem. The ability of this method to perform well depends heavily on the proper choice of the pseudocompressibility constant  $\beta$ . This paper has presented an analysis of the effect on the calculations of using different values of  $\beta$ , and on this basis has presented guidelines for the proper choice of  $\beta$ . These guidelines are substantiated with example calculations. The accuracy of the method is affected by the amount of smoothing used, and whereas the algorithm requires some smoothing for stability, by decreasing the smoothing as a steady state is reached, accurate solutions to the incompressible Navier-Stokes equations can be obtained. The computing time has been shown to be reasonable when compared to another method which used a similar algorithm for its solution process. Finally, the code was shown to be able to solve a three-dimensional problem with some very interesting and complex fluid phenomena.

Such a code could be a valuable tool for many engineering problems, particularly if some more study of the time-accuracy of the method were done. It is possible that an iterative-type scheme could help reduce the divergence of the velocity field at the end of each time-step. Such a scheme should be similar to the fractional step method iterations shown in equations (1.1) and (1.2). This iteration would be very much like artificial compressibility in that there would be artificial pressure waves distributing the pressure. If the iterations were carried out until they converged, this would correspond to the waves dying out completely, and the flow would be divergence-free. However, instead of iterating until the flow field is completely divergent-free, the iterations could be allowed to stop after the divergence of the velocity has been reduced by an order of magnitude or so. Through testing, a criteria could be found as to how much iterating must be done to get a desired level of quantitative accuracy. In other words, the way for the artificial compressibility to obtain time-accurate answers is to let the pressure waves travel further for each time-step than they do in the current one-step formulation.

## REFERENCES

1. Kutler, P.: A Perspective of Theoretical and Applied Computational Fluid Dynamics. AIAA Paper 83-0037, Reno, Nev., 1983.
2. Roux, B.; Bontoux, P.; Loc, T.P.; and Daube, O.: Optimization of Hermitian Methods for Navier-Stokes equations in the Vorticity and Stream-function Formulation. Approximation Methods for Navier-Stokes Problems; Proceedings of the Symposium, Paderborn, West Germany, Berlin, Springer-Verlag, 1980, p. 450-468.
3. Quartapelle, L.: Vorticity Conditioning in the Computation of Two Dimensional Viscous Flows. J. Comp. Phys., vol. 40, April, 1980, pp. 450-468.
4. Agarwal, R. K.: A Forth-Order-Accurate Compact Differencing Scheme for Steady Navier-Stokes Equations. AIAA Paper 82-0977, St. Louis, MO, 1982.
5. Mehta, U. B.: Dynamic Stall of an Oscillating Airfoil. Paper No. 23, AGARD Conference Proceedings No. 227, Ottawa, Canada, Sept. 1977.
6. Shang, J. S.; Buning, P. G.; Hankey, W. L.; and Wirth, M. C.: Performance of a Vectorized Three-Dimensional Navier-Stokes Code on the Cray-1 Computer. AIAA J., vol. 18, no. 9, Sept. 1980, pp. 1073-1079.
7. Hung, C. M.; and Kordulla, W.: A Time-Split Finite-Volume Algorithm for Three-Dimensional Flow-Field Simulation. AIAA Paper 83-1957, Danver, Mass, 1983.
8. Pulliam, T. H.; and Steger, J. L.: Implicit Finite-Difference Simulations of Three-Dimensional Compressible Flow. AIAA J., vol. 18, no. 2, 1980, pp. 159-167.
9. Briley, W. R.; and McDonald, H.: Solution of the Three-Dimensional Compressible Navier-Stokes Equations by an Implicit Technique. Proceedings of Fourth International Conference on Numerical Methods in Fluid Dynamics; Lecture Notes in Physics, vol. 35, Springer-Verlag, New York, 1975, pp. 105-110.
10. Harlow, F. H.; and Welch, J. E.: Numerical Calculation of Time Dependent Viscous Incompressible Flow with Free Surface. Physics of Fluids, vol. 8, no. 12, Dec. 1965, pp. 2182-2189.
11. Williams, G. P.: Numerical Integration of the Three-Dimensional Navier-Stokes Equations for Incompressible Flow. J. Fluid Mech., vol. 37, 1969, pp. 727-750.
12. Donovan, L. F.: A Numerical Solution of Unsteady Flow in a Two-Dimensional Square Cavity. AIAA J., vol. 8, no. 3, 1970, pp. 524-529.
13. Hodge, J. K.: Numerical Solution of Incompressible Laminar Flow About Arbitrary Bodies in Body-Fitted Curvilinear Coordinates. Ph.D. Dissertation, Mississippi State University, Dec., 1975.
14. Ghia, K. N.; Hankey, W. L.; and Hodge, J. K.: Study of Incompressible Navier-Stokes Equations in Primitive Variables Using Implicit Numerical Technique. AIAA Paper 77-648, Albuquerque, NM, 1977.
15. Loc, T. P.: Numerical Analysis of Unsteady Secondary Vortices Generated by an Impulsively Started Circular Cylinder. J. of Fluid Mech., vol. 100, 1980, pp. 111-128.

16. Hegna, H. A.: The NUMerical Solution of the Navier-Stokes Equations for Incompressible Turbulent Flow over Airfoils. AFWAL-TR-81-3053, Oct., 1981.
17. Bernard, R. S.; and Thompson, J. F.: Approximate Factorization with an Elliptic Pressure Solver for Incompressible Flow. AIAA Paper 82-0978, St. Louis, MO, 1982.
18. Chorin, A. J.: Numerical Soltuion of The Navier-Stokes Equations. Math. and Computers, vol. 22, 1968, pp. 745-762.
19. Chorin, A. J.: On the Convergence of Discrete Approximations to the Navier-Stokes Equations. Mathematics of Comput., Vol. 23, No. 106, April, 1969, pp. 341-353.
20. Temam, R., Navier-Stokes Equations: Theory and Numerical Analysis, vol. 2, North-Holland Pub. Co., Amsterdam, 1977, pp. 395-425.
21. Kim, J.; and Moin, P.: Application of a Fractional-Step Method to Incompressible Navier-Stokes Equation. NASA TM 85898, March, 1984.
22. Chorin, A. J.: A Numerical Method for Solving Incompressible Viscous Flow Problems. J. Comp. Phys., vol. 2, 1967, pp. 12-26.
23. Steger, J. L.; and Kutler, P.: Implicit Finite-Difference Procedures for the Computation of Vortex Wakes. AIAA J., vol. 15, no. 4, April, 1977, pp. 581-590.
24. Beam, R. M.; and Warming, R. F.: An Implicit Finite-Difference Algorithm for Hyperbolic Systems in Conservation-Law Form. J. of Comp. Phys., vol. 22, Sept. 1976, pp. 87-110.
25. Kwak, D.; Chang, J. L. C.; Shanks, S. P.; and Chakravarthy, S.: An Incompressible Navier-Stokes Flow Solver in Three-Dimensional Curvilinear Coordinate System Using Primitive Variables. AIAA Paper 84-0253, Reno, Nev., Jan. 1984.
26. Kwak, D.; Chang, J. L. C.; and Shanks, S. P.: A Solution Procedure for Three-Dimensional Incompressible Navier-Stokes Equation and Its Application. Nineth International Conference on Numerical Methods in Fluid Dynamics, C.E.N. Saclay, France, June 25-29, 1984.
27. Chang, J. L. C.; Kwak, D.; and Dao, S. C.: A Three Dimensional Incompressible Flow Simulation Method and its Application to the Space Shuttle Main Engine, Part 1, Laminar Flow. AIAA Paper 85-0175, Reno, Nev., Jan, 1985.
28. Chang, J. L. C.; and Kwak, D.: On the Method of Pseudo Compressibility for Numerically Solving Incompressible Flows. AIAA Paper 84-0252, Reno, Nev., 1984.
29. Armaly, B. F.; Durst, F.; Pereira, J. C. F.; and Schönung, B.: Experimental and Theoretical Investigation of Backward Facing Step Flow. J. Fluid Mech., vol. 127, pp. 473-496, 1983.
30. Morkovin, M. V.: Flow Around Circular Cylinder; A Kaleidoscope of Challenging Fluid Phenomena. Symposium On Fully Separated Flows, Hansen, A. G., ed., ASME, New York, 1964, pp. 102-118.
31. Nagata, H.; Matsui, T.; and Yasuda, H., JSME paper 45-197, 1297, 1979.
32. Bouard, R.; and Coutanceau, M.: The Early Stage of Development of The Wake Behind an Impulsively Started Cylinder For  $40 < Re < 10^4$ . J. Fluid Mech., vol. 101, part 3, pp. 583-607, 1980.

33. Honji, H.; and Taneda, S.: Unsteady Flow Past a Circular Cylinder. J. Phys. Soc. of Japan, vol. 27, p. 1668, 1969.
34. Taneda, S.: Visualization Experiments on Unsteady Viscous Flows Around Cylinders and Plates. In underrstepRécentes Recherches Sur Les Limites Instationnaires, vol. 2, Eichelbrenner, E. A., ed., p. 1165, Laval University Press, Quebec, 1972.
35. Thoman, D. C.; and Szewczyk, A. A.: Time-dependant Viscous Flow Over a Circular Cylinder. Phys. Fluids Suppl., vol. 12, No. 2, p. 76, 1969.
36. Loc, Ta Phuoc: Numerical Analysis of Unsteady Secondary Vorticies generated by an impulsively started Circular Cylinder. J. of Fluid Mech., vol. 100, pp. 111-128, 1980.
37. Lecointe, Y.; and Piquet, J.: On the Use of Several Compact Methods For The Study of Unsteady Incompressible Viscous Flow Round A Circular Cylinder. Computers and Fluids, vol. 12, no. 4, pp. 255-280, 1984.

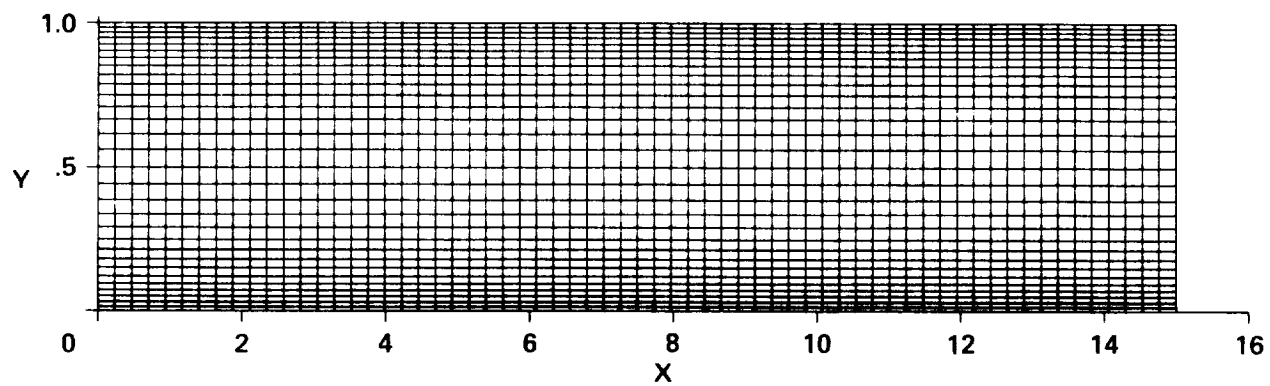


Figure 1 Grid used for channel flow.

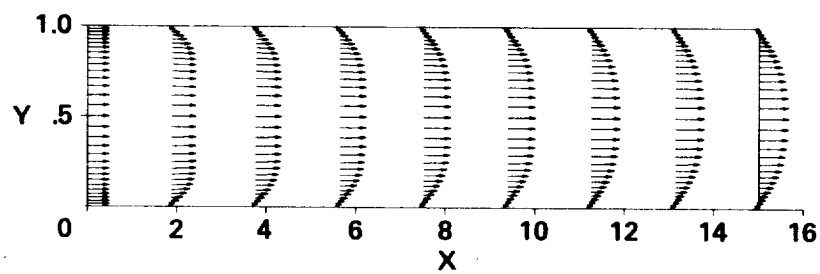


Figure 2 Velocity profiles for  $\beta = 5.0$ .



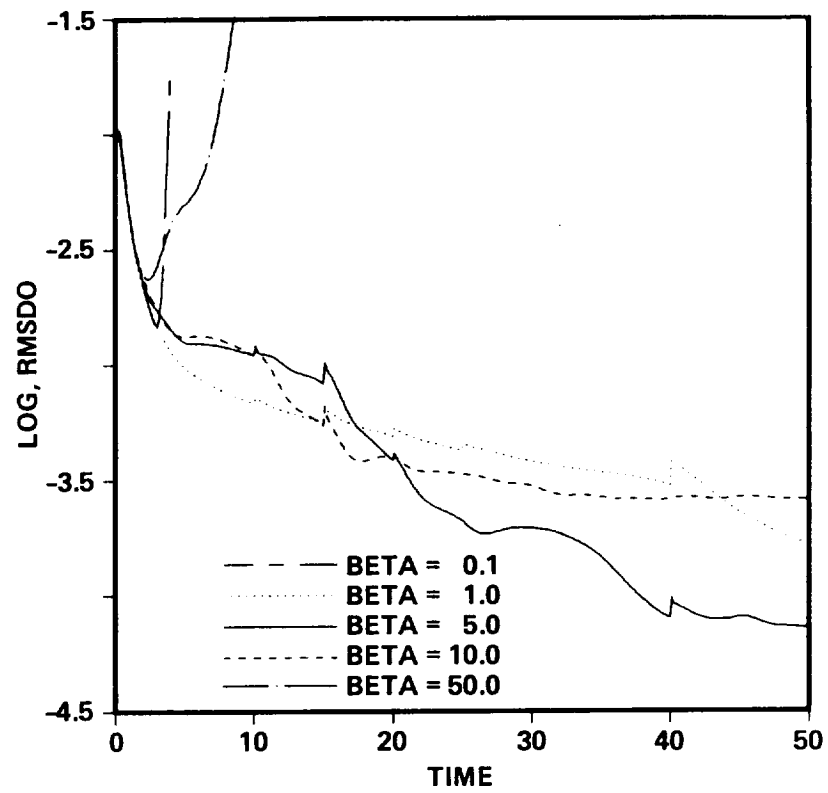


Figure 3 Convergence rate for various values of  $\beta$ .

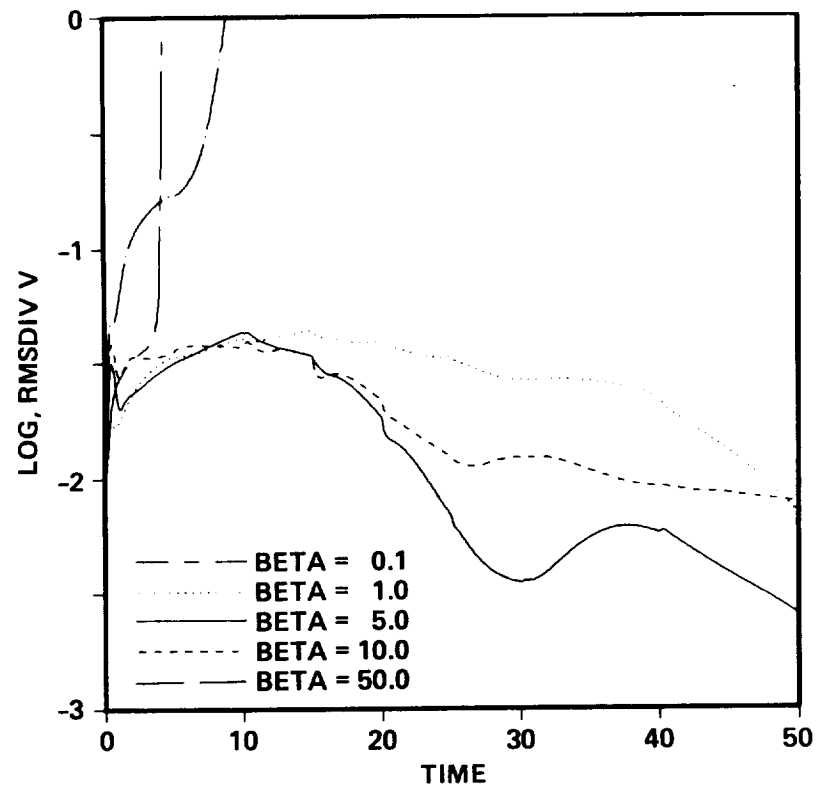


Figure 4 Divergence of the velocity field versus time.

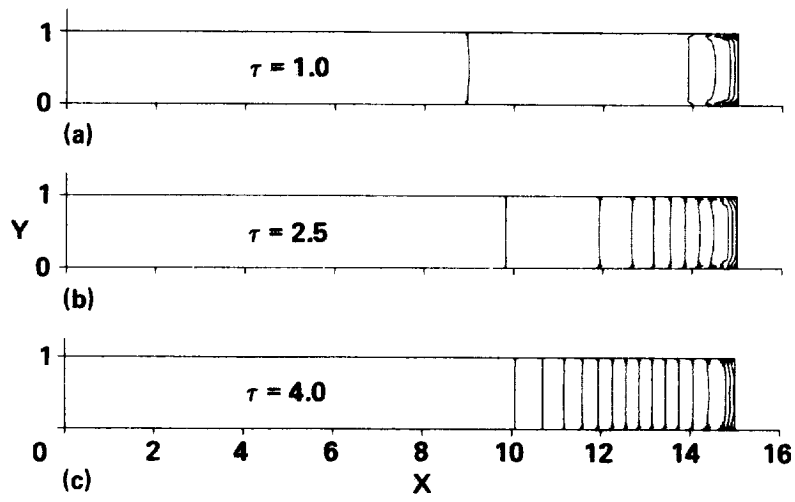


Figure 5 Pressure contours for  $\beta = 5.0$  at  $t = 1, 2.5$ , and  $4$ .

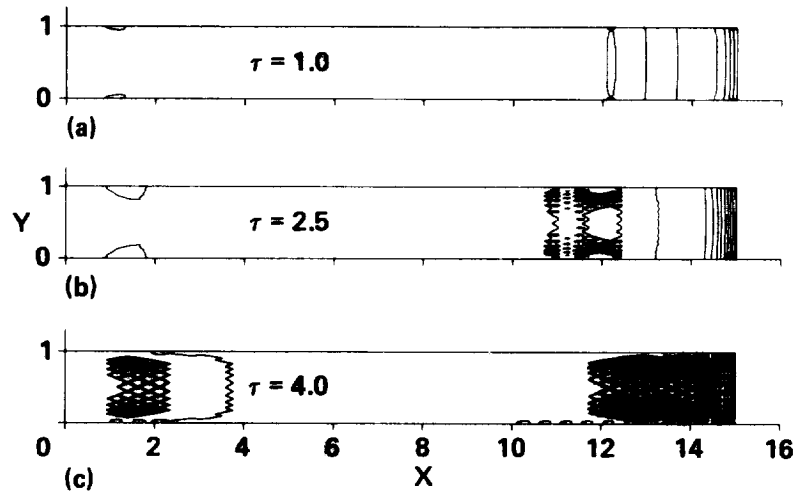


Figure 6 Pressure contours for  $\beta = 0.1$  at  $t = 1, 2.5$ , and  $4$ .

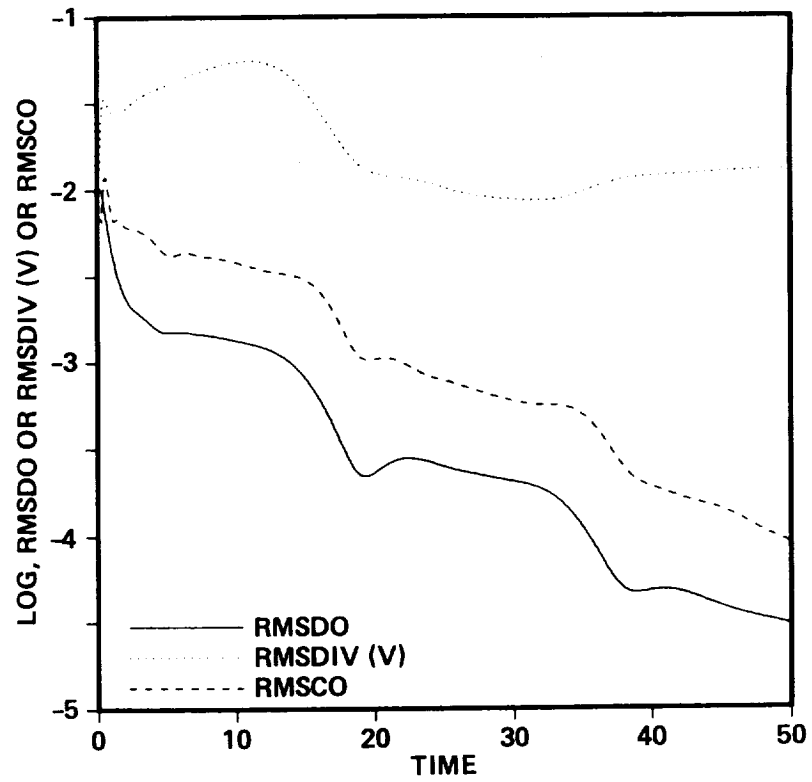


Figure 7 Effect of decreasing smoothing with time  $\alpha = 0.01$ .

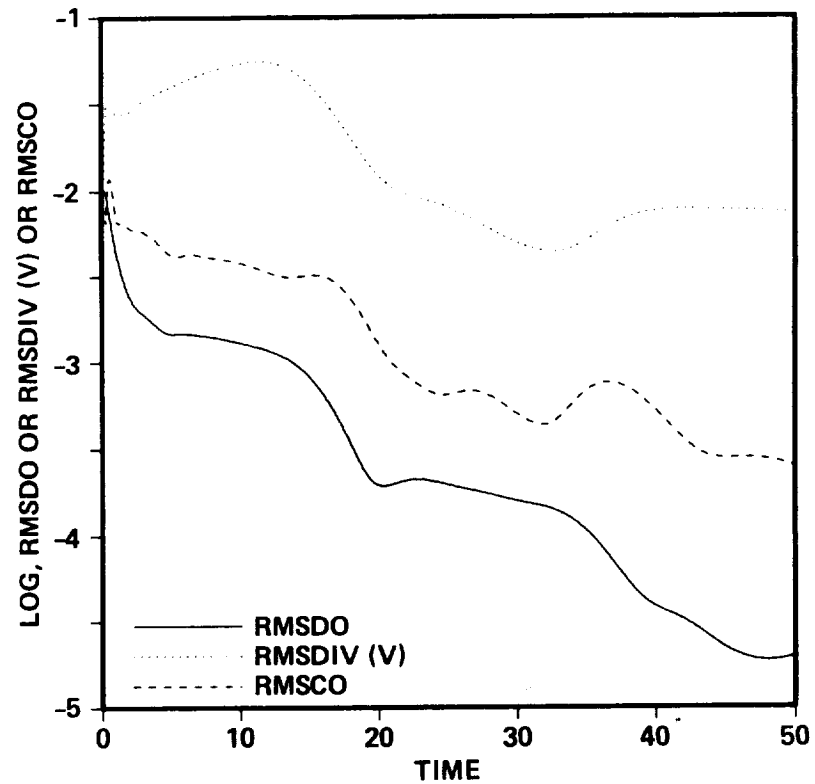


Figure 8 Effect of decreasing smoothing with time  $\alpha = 0.05$ .

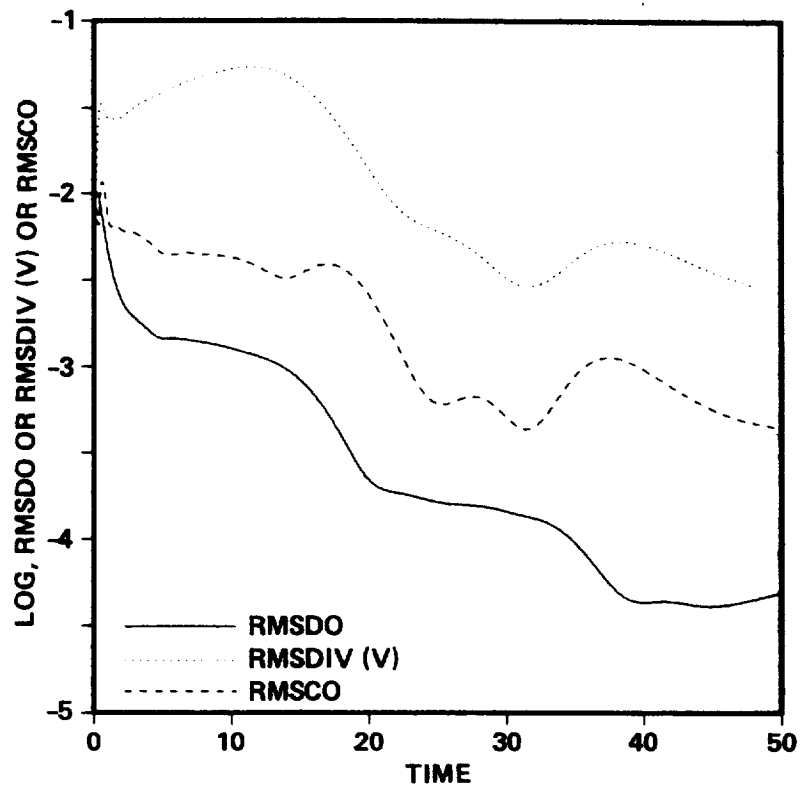


Figure 9 Effect of decreasing smoothing with time  $\alpha = 0.1$ .

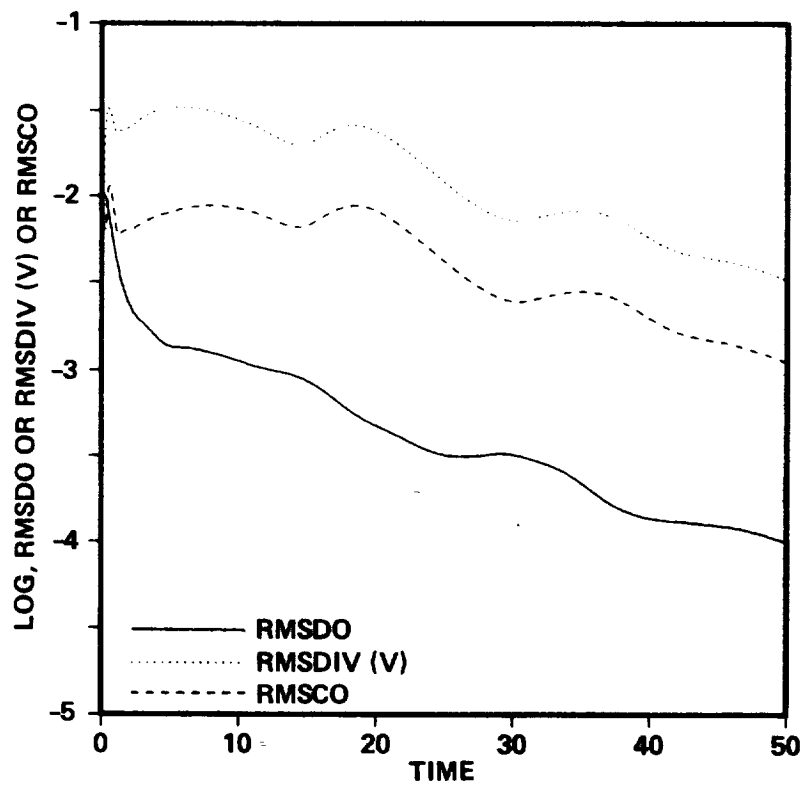


Figure 10 Effect of decreasing smoothing with time  $\alpha = 0.5$ .

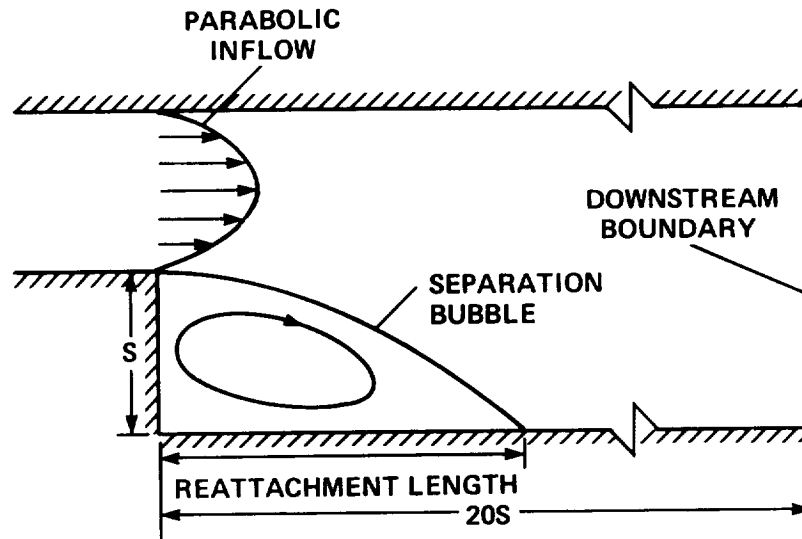


Figure 11 Flow over a backward-facing step.

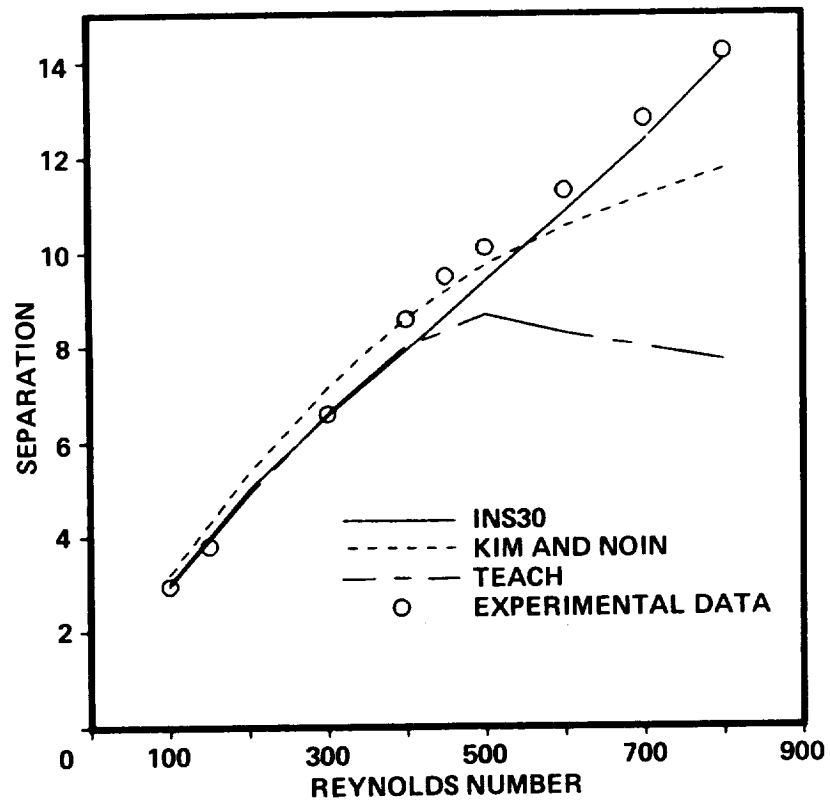


Figure 12 Reattachment length versus Reynolds number.

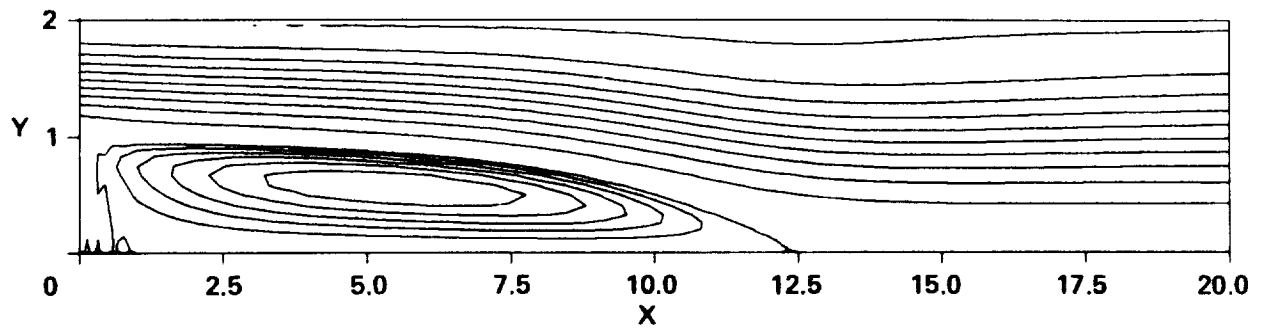


Figure 13 Streamlines for backstep flow at  $Re = 700$ .

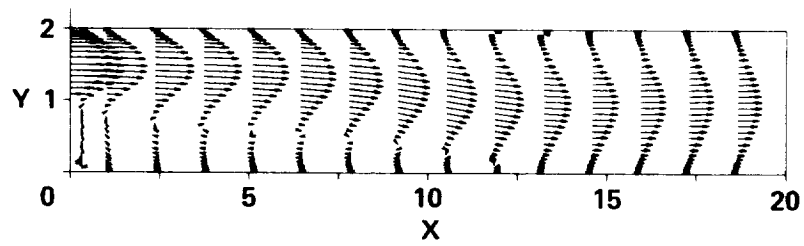


Figure 14 Velocity vectors for backstep flow at  $Re = 700$ .

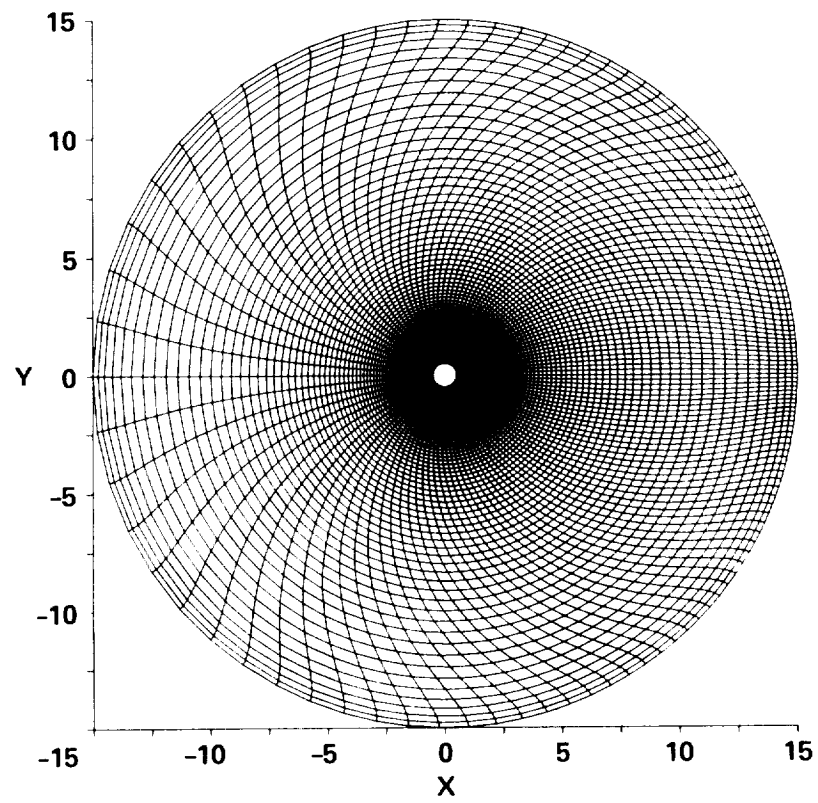
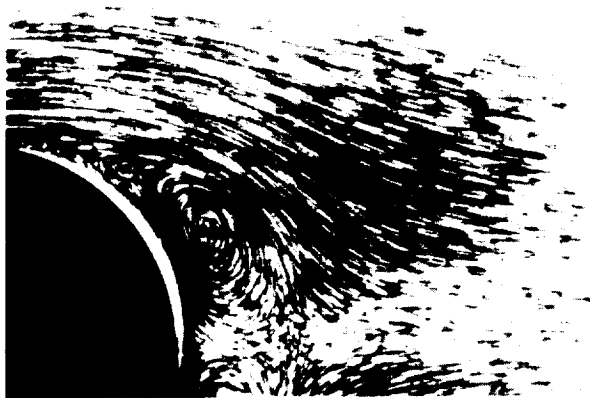
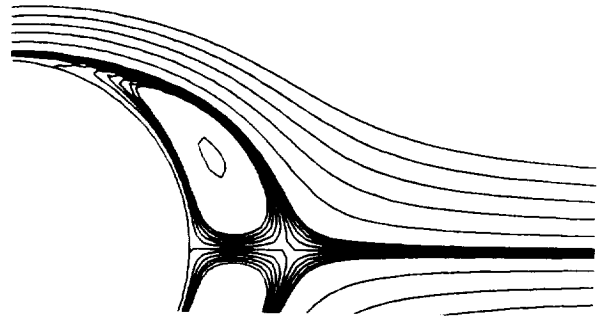


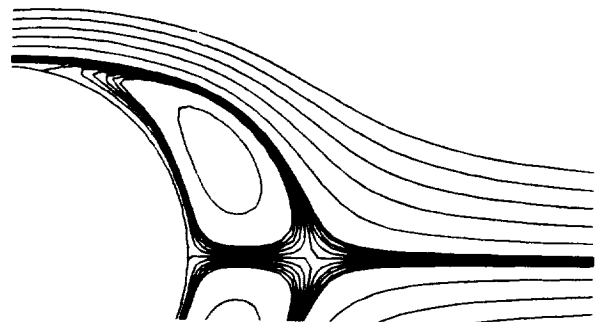
Figure 15 Grid for a circular cylinder.



T=1.1



T=1.3



T=1.9

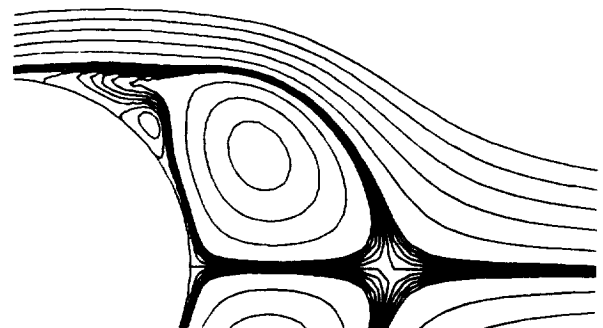
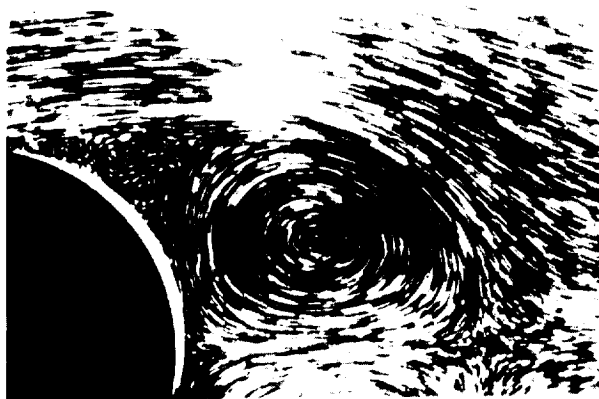
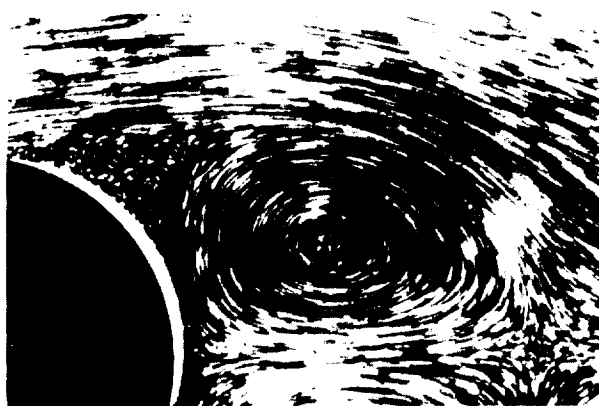
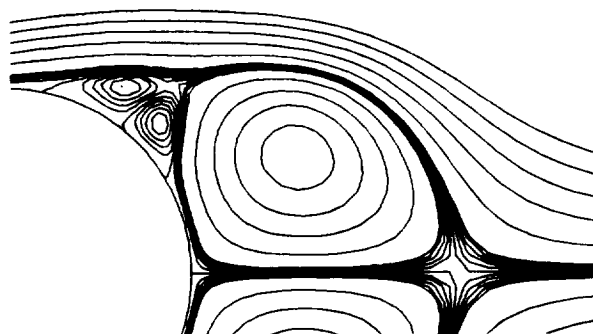


Figure 16a Experimental pictures and computational streamlines for an impulsively started cylinder at  $\tau = 1.1, 1.3$ , and  $1.9$ .

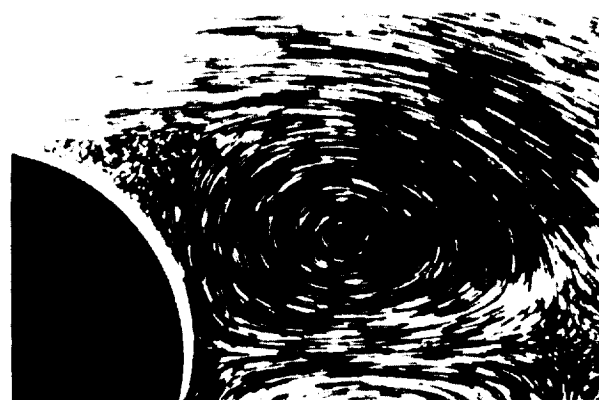
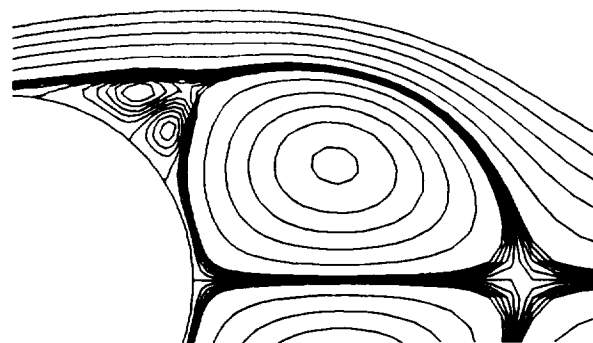




T=2.4



T=2.9



T=3.1

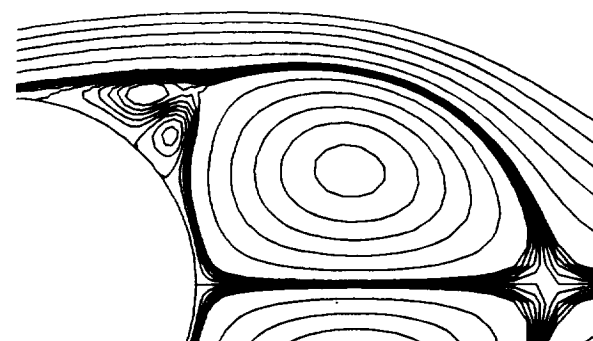


Figure 16b Experimental pictures and computational streamlines for an impulsively started cylinder at  $\tau = 2.4, 2.9$ , and  $3.1$ .

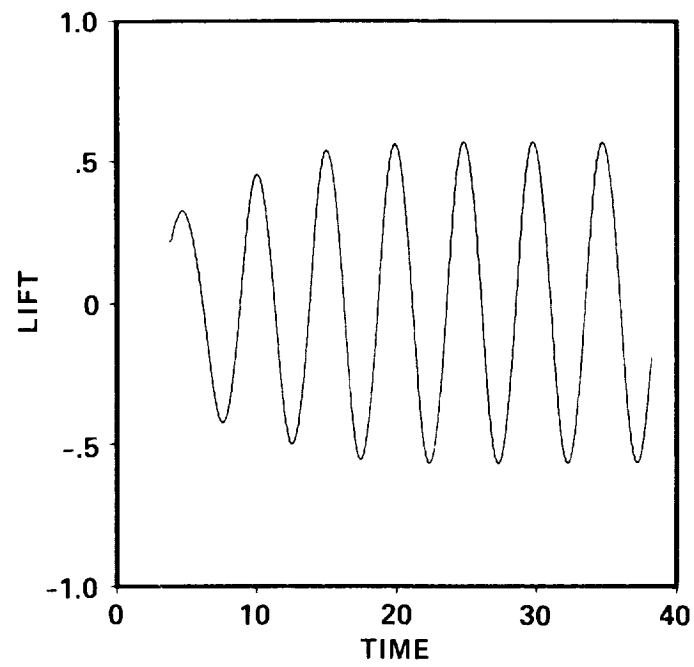


Figure 17 Lift versus time for periodic flow over a cylinder.

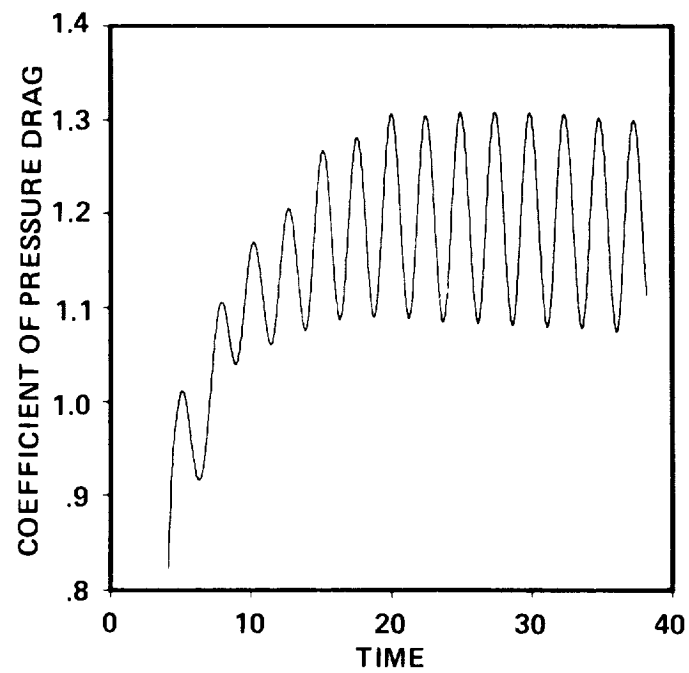


Figure 18 Coefficient of pressure drag versus time.

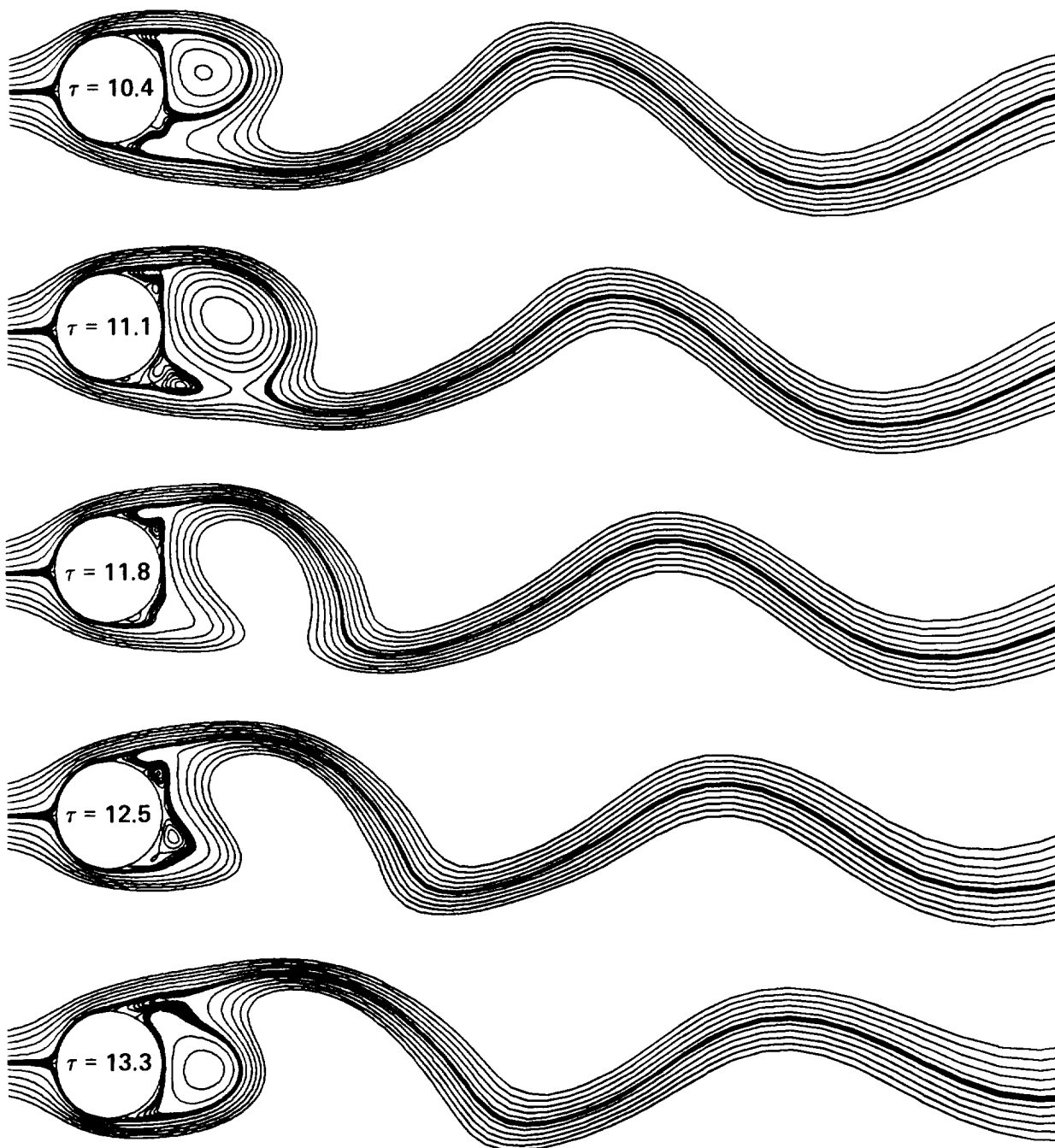


Figure 19 Streamlines of periodic flow past a cylinder.

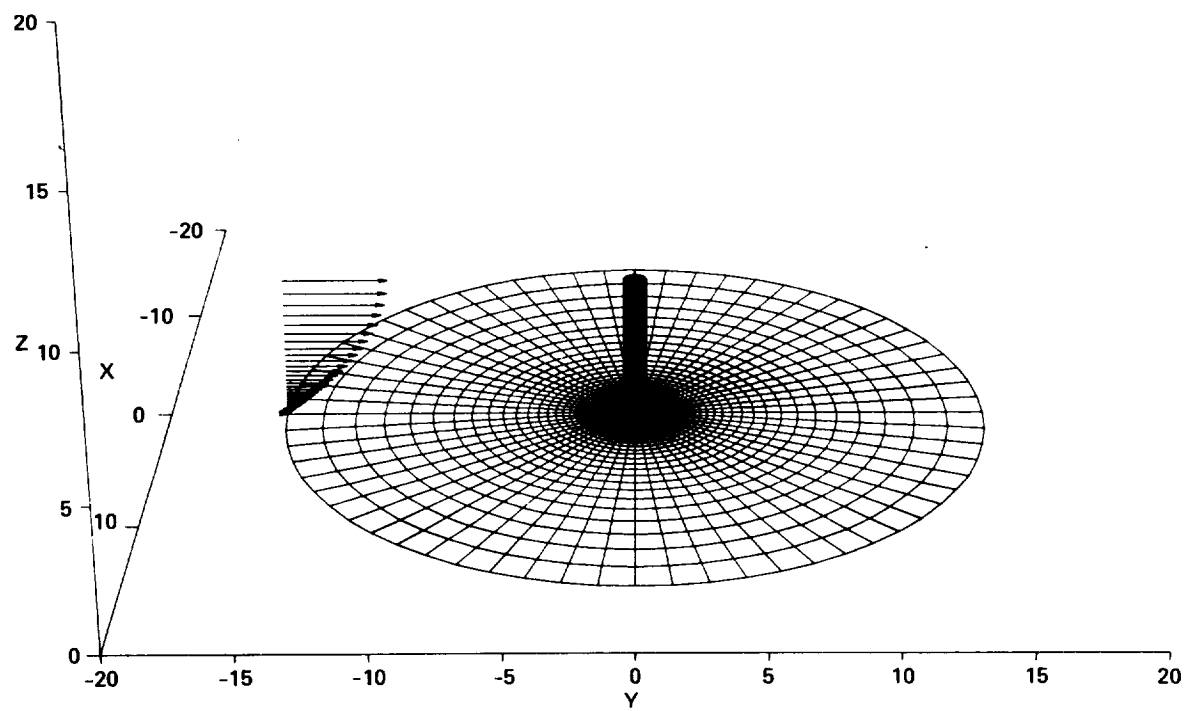


Figure 20 Grid for a cylinder on a flat plate.

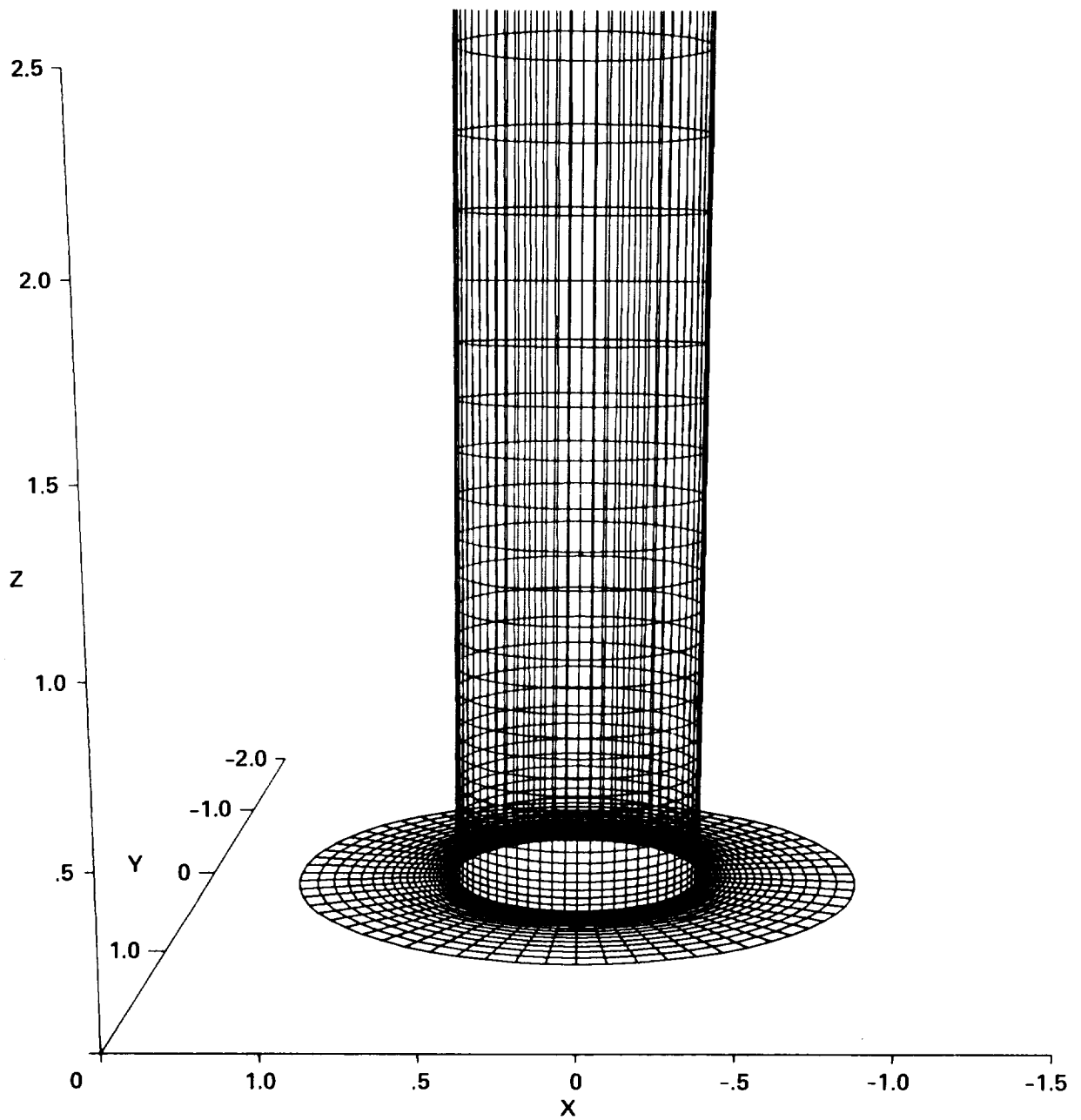


Figure 21 Grid spacing near cylinder-plate junction.

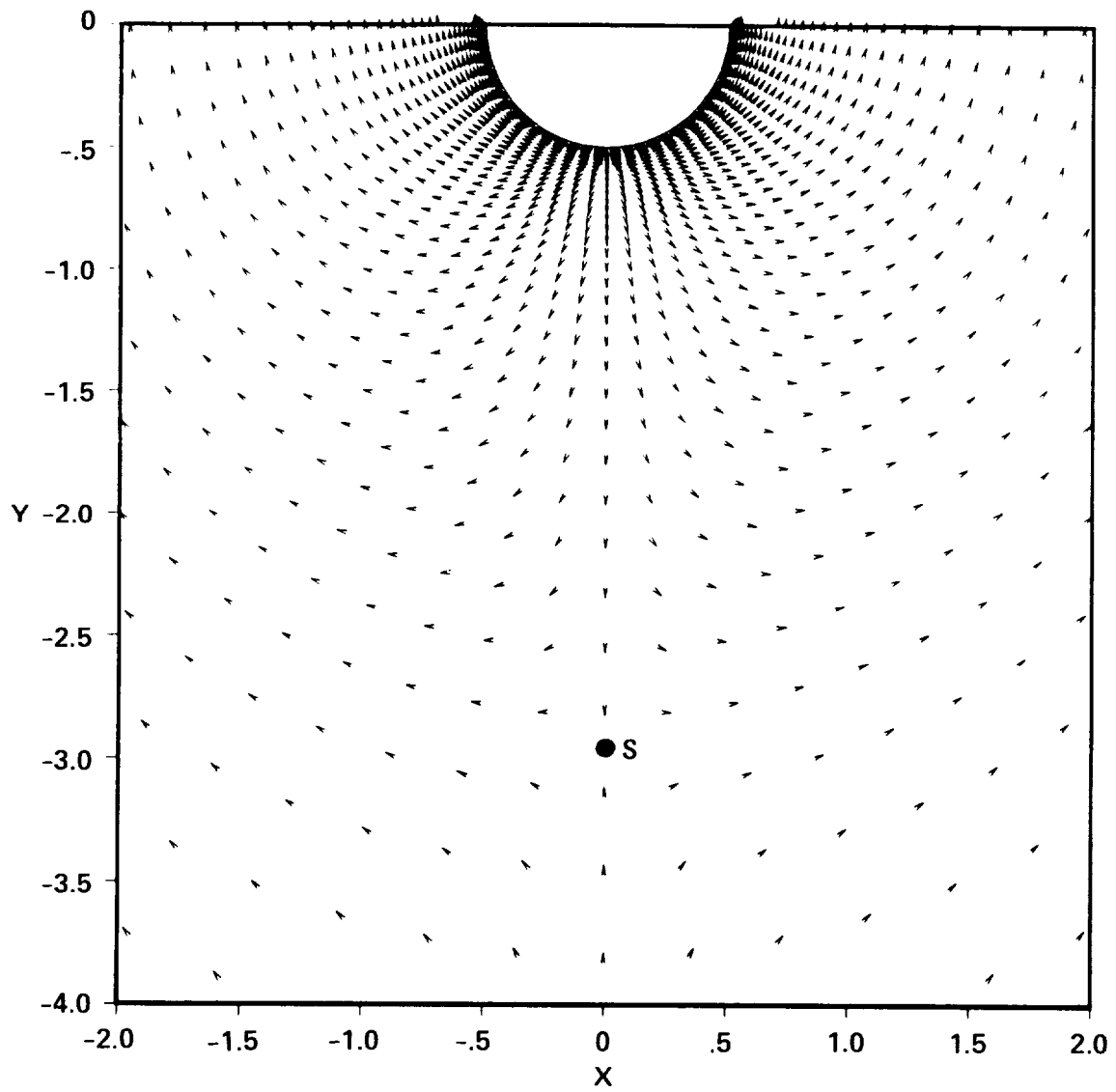


Figure 22 Velocity vectors showing saddle point separation.

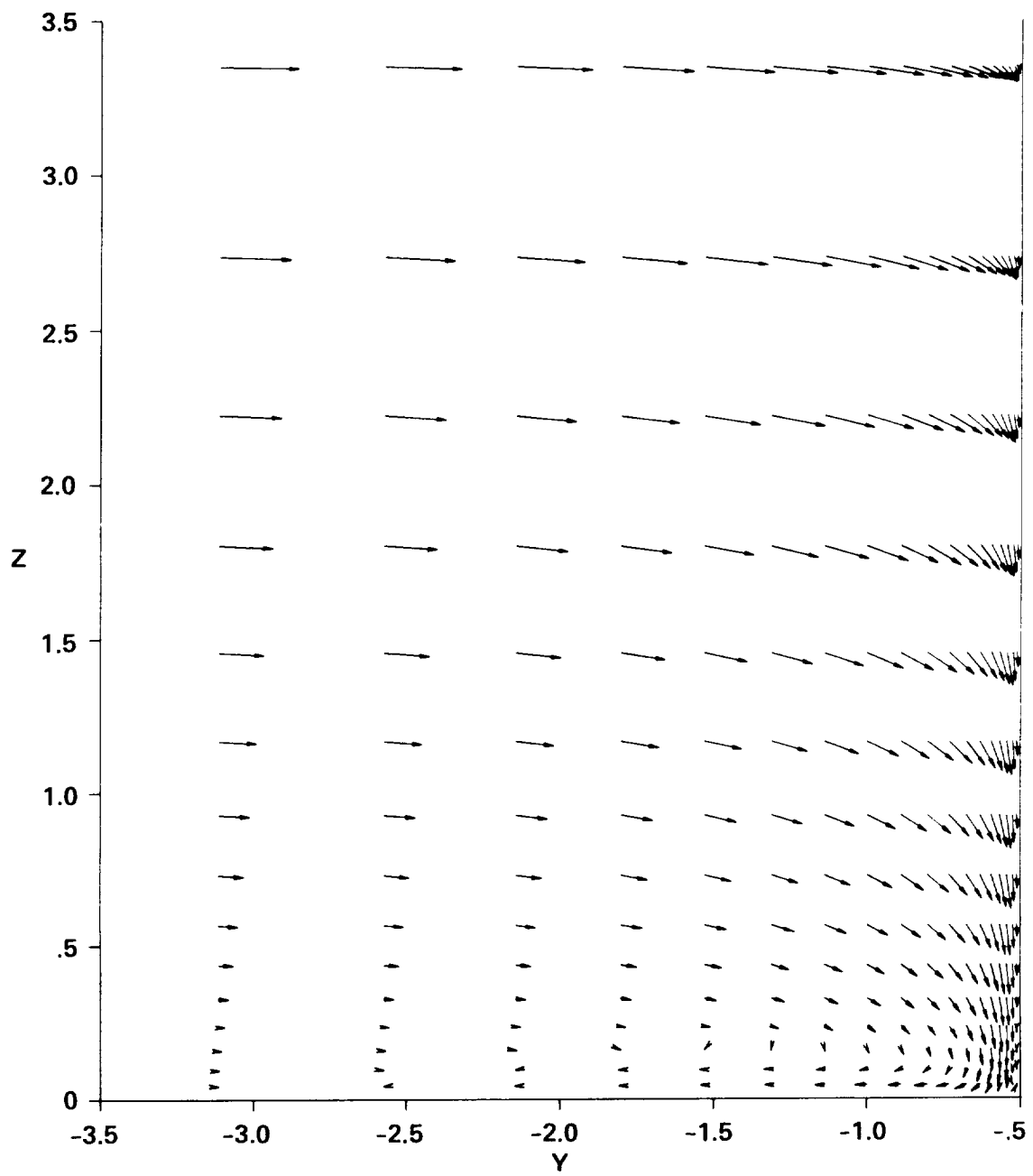


Figure 23 Side view showing saddle point separation and nodal point of reattachment.

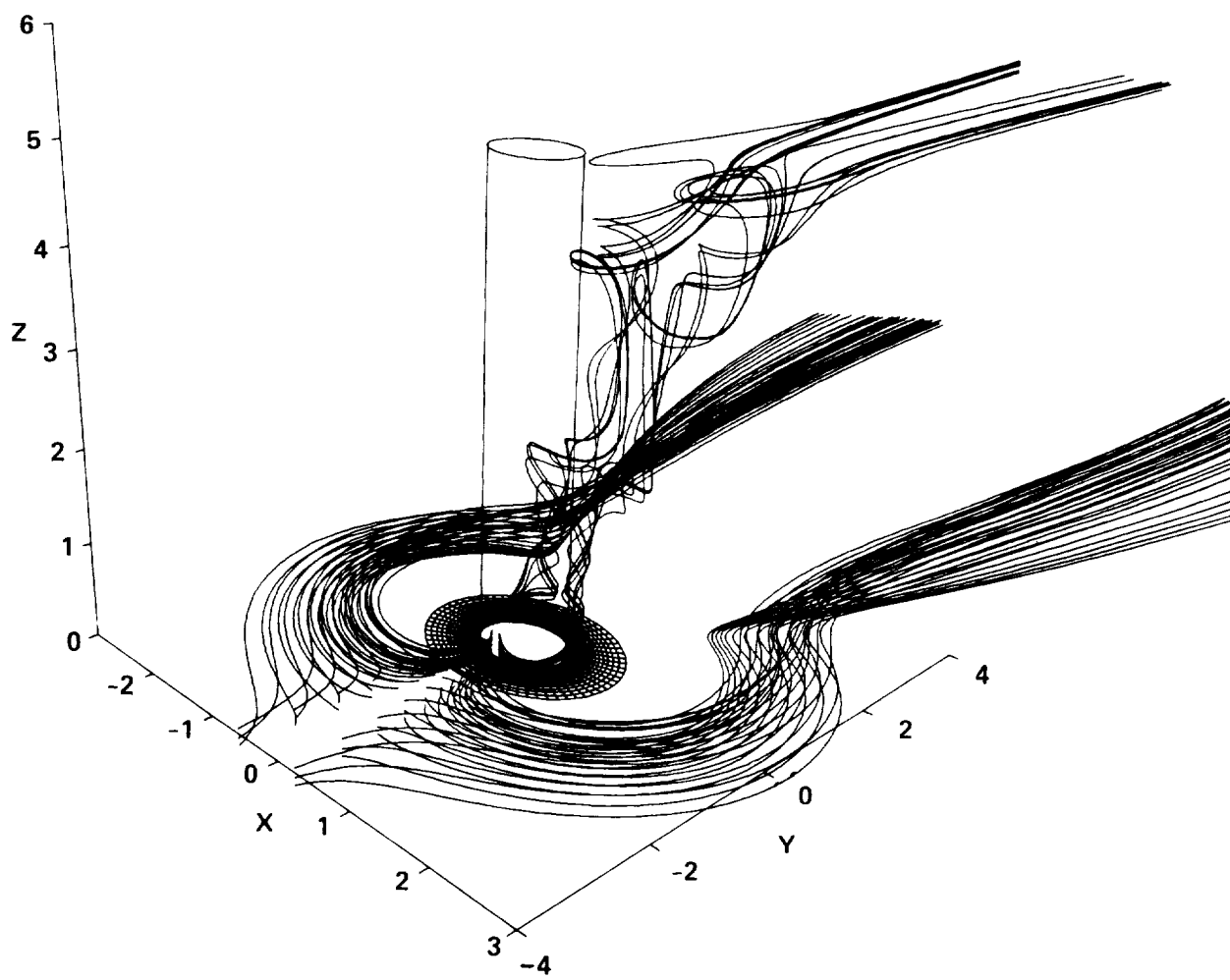


Figure 24 Particle traces.



1. Report No. NASA TM-86840		2. Government Accession No.		3. Recipient's Catalog No.	
4. Title and Subtitle NUMERICAL SOLUTION OF THE INCOMPRESSIBLE NAVIER-STOKES EQUATIONS IN THREE-DIMENSIONAL GENERALIZED CURVILINEAR COORDINATES				5. Report Date January 1986	
				6. Performing Organization Code	
7. Author(s) Stuart E. Rogers and Dochan Kwak, and James L. C. Chang (Rockwell International, Canoga Park, California)				8. Performing Organization Report No. 85413	
				10. Work Unit No.	
9. Performing Organization Name and Address Ames Research Center Moffett Field, CA 94035				11. Contract or Grant No.	
				13. Type of Report and Period Covered Technical Memorandum	
12. Sponsoring Agency Name and Address National Aeronautics and Space Administration Washington, DC 20546				14. Sponsoring Agency Code 505-60	
15. Supplementary Notes Point of Contact: Stuart Rogers, Ames Research Center, M/S 202A-14, Moffett Field, CA 94035 (415) 694-6740 or FTS 464-6740					
16. Abstract Numerically solving the incompressible Navier-Stokes equations is known to be time-consuming and expensive. Testing of the INS3D computer code, which solves these equations with the use of the pseudocompressibility method, shows this method to be an efficient way to obtain the steady-state solution. The effects of the waves introduced by the pseudocompressibility method are analyzed and criteria are set and tested for the choice of the pseudocompressibility parameter which governs the artificial sound speed. The code is tested using laminar flow over a two-dimensional backward-facing step, and laminar flow over a two-dimensional circular cylinder. The results of the computations over the backward-facing step are in excellent agreement with experimental results. The transient solution of the flow over the cylinder impulsively started from rest is in good agreement with experimental results. However, the computed frequency of periodic shedding of vortices behind the cylinder is not in agreement with the experimental value. For a three-dimensional test case, computations were conducted for a cylinder-end wall junction. The saddle point separation and horseshoe vortex system appear in the computed flow field. The solution also shows secondary vortex filaments which wrap around the cylinder and spiral up in the wake.					
17. Key Words (Suggested by Author(s)) Computational fluid dynamics Incompressible Navier-Stokes equations Pseudocompressibility Backward-facing step Circular cylinder				18. Distribution Statement Unlimited  Subject category - 34	
19. Security Classif. (of this report) Unclassified		20. Security Classif. (of this page) Unclassified		21. No. of Pages 47	
22. Price*					

